Journal of Geophysical Research: Earth Surface

RESEARCH ARTICLE
10.1029/2017JF004341

Key Points:
- A new approach for the study of surging based on crevassing is introduced bringing together geostatistical characterization and modeling
- Crevasse-based model-data comparisons help optimize unknown model parameters such as the basal friction coefficient
- Bed topography is an important constraint in modeling the surge process

Correspondence to:
T. Trantow,
trantow@colorado.edu

Citation:
Trantow, T., & Herzfeld, U. C. (2018). Crevasses as indicators of surge dynamics in the Bering Bagley Glacier System, Alaska: Numerical experiments and comparison to image data analysis. *Journal of Geophysical Research: Earth Surface*, *123*, 1615–1637. https://doi.org/10.1029/2017JF004341

Received 8 MAY 2017
Accepted 25 MAY 2018
Accepted article online 19 JUN 2018
Published online 4 AUG 2018

Crevasses as Indicators of Surge Dynamics in the Bering Bagley Glacier System, Alaska: Numerical Experiments and Comparison to Image Data Analysis

Thomas Trantow[1] **and Ute C. Herzfeld**[1,2]

[1]Department of Electrical, Computer and Energy Engineering, University of Colorado, CO Boulder, USA, [2]Cooperative Institute for Research in Environmental Sciences, Boulder, CO, USA

Abstract One of the largest sources of uncertainty in sea level rise prediction is glacial acceleration, of which the surge phenomenon is the least understood type. The surge of the Bering Bagley Glacier System (BBGS), Alaska, in 2011–2013 has provided a rare opportunity to study the surge phenomenon in a large and complex glacier system. A surge results in widespread crevassing throughout the glacier system complicating many traditional techniques used to study glacier dynamics. In this paper, we utilize crevassing as a means to investigate the recent BBGS surge through numerical modeling and geostatistical data analysis. Following the principles of structural glaciology, image-based crevasse characterizations are obtained through geostatistical methods applied to Landsat-7 data, supplemented by airborne field observations. On the modeling side, a 3-D full-Stokes finite element model of the BBGS is developed and applied to investigate ice dynamics and surface structures during the recent surge. A von Mises criterion is adopted to simulate crevassing at the glacier surface, oriented along the axes of maximum principal tensile stress. To facilitate evaluation of model- and data-derived crevasse characteristics, three different comparison methods are introduced. General agreement in the model-data comparisons indicates that the model has the ability to represent the BBGS system during peak acceleration. The crevasse-based approach is also employed to optimize the basal sliding parameter and the von Mises stress threshold in the model. Results further indicate that bed topography is an important constraint in modeling the surge process.

1. Introduction

Glacial acceleration has been identified as one of the two main sources of uncertainty in global sea level rise assessment in the current realm of climatic warming, as established in the Fifth Assessment Report of the Intergovernmental Panel on Climate Change (Stocker et al., 2013). Surging is one of four types of glacial acceleration and the one that has seen the least amount of research, largely due to relative paucity of observations. Fast-flowing glaciers have been categorized with respect to their acceleration type, including tidewater glaciers with long periods of velocity changes (~1000 years), surge glaciers with quasi-cyclic changes on the order of 10–100 years, always-fast-flowing ice streams, ice streams with a state-switching behavior and combinations thereof (Clarke, 1987; Truffer & Echelmeyer, 2003). A surge-type glacier cycles quasi-periodically between a long quiescent phase of regular flow speeds and gradual retreat, and a short surge phase when flow speeds accelerate to 10–100 times their normal velocity, with cycle length specific to the individual glacier, but typically on the order of decades. Surge-type glaciers are present in many different parts of the Earth but are relatively sparse (Dolgushin & Osipova, 1975; Herzfeld, 1998; Meier & Post, 1969; Sevestre & Benn, 2015). The state of knowledge on the surge process has been summarized by Meier and Post (1969), by Raymond (1987), and by Harrison and Post (2003), with each concluding that the physics of the surge process is complex and not fully understood.

The 2011–2013 surge in the Bering Bagley Glacier System (BBGS), Alaska, has provided an opportunity for data collection and analysis of the surge phenomenon in a large and complex glacier system (Herzfeld, McDonald, Stachura, et al., 2013; Herzfeld, McDonald, & Weltman, 2013; Trantow & Herzfeld, 2016). The BBGS is one of the largest glacial systems outside of Greenland and Antarctica and the largest temperate surge-type glacier on Earth (Molnia, 2008). We collected airborne altimeter and image data during four field campaigns to the BBGS

in 2011 – 2013 (see Herzfeld, McDonald, Stachura, et al., 2013; Herzfeld, McDonald, & Weltman, 2013). However, much of our understanding of surges stems from investigations of small glaciers (e.g., Clarke et al., 1984; Eisen et al., 2001, 2005; Flowers & Clarke, 2000, 2002a, 2002b; Flowers et al., 2011; Harrison et al., 2008; Humphrey et al., 1986; Jay-Allemand et al., 2011; Kamb et al., 1985; Raymond, 1987), which can be instrumented to get reasonable field data coverage. Because the BBGS is too large to allow meaningful data collection on the ground, we investigate the surge using satellite data together with airborne and image data collected during our field campaigns. The BBGS is complex because it includes surge-type and nonsurge-type glaciers. A surge in the BBGS does not affect the entire surge-type part of the glacier system at the same time. Instead, several characteristic parts of the surge process, such as surge initiation or reinitiation, start and end during certain surge phases, which occur at different locations and times, sometimes a year apart. The BBGS shares this property of complexity with sections of the margins of the Greenland and Antarctic ice sheets, where surge-type glaciers are found neighboring nonsurge-type glaciers and continually fast-moving ice streams (Herzfeld, 2004; Jiskoot, 1999; Sevestre & Benn, 2015). Hence, the BBGS plays an important role in understanding glacier surging, and more generally, the role of glacial acceleration in sea level rise assessment.

The rapid ice-surface deformation that occurs during a surge causes methods that depend on correlation, such as feature tracking methods used to calculate surface velocity, to fail during sudden and complex acceleration events (e.g., for Bering Glacier, Fatland & Lingle, 1998, in 1994 or Burgess et al., 2013, in 2011). In this paper, an approach is taken that is motivated by the observation of the most conspicuous manifestation of a surge: that of surface crevassing. The advantage of investigating crevassing is that it is a tractable variable during complex dynamics and complex deformation and requires only a single observation for analysis. The main BBGS surge phase in early-2011, described in section 2, is used as a case study since a broad range of fresh crevassing occurred during this time. We introduce a new approach in section 3 that involves comparisons of crevassing determined from both observations and numerical modeling. In section 4, we introduce our method for characterizing crevasses using both geostatistical and manual characterization of satellite optical imagery. In section 5, we describe the approach to modeling crevassing during a surge, which involves analysis of surface stresses and a crevasse formation criterion. Observed and modeled crevasses are then compared in section 6 in terms of crevasse location, orientation, and crevassity. We introduce the term crevassity as a measure of the void fraction in glacier ice as a material, akin to porosity. Crevassity is used as a general term to describe the magnitude and complexity of the overall deformation at a given location and is estimated using modeled surface stresses and observed surface roughness. A map comparison method is employed to determine the relationship between the surface stress, encapsulated by the scalar von Mises measure, and the observed surface roughness given by the geostatistical parameter *pond*. In section 7, we use the crevasse-related model-data comparisons to constrain and optimize the basal friction parameter and the von Mises stress threshold. The paper thus has three objectives: (1) to numerically simulate the observed crevassing that formed during the early-2011 phase of the BBGS surge, (2) to demonstrate that crevassing can be employed as a means to understand the physical processes of glacial acceleration through numerical modeling and novel crevasse-based model-data comparison techniques, and (3) to investigate the state of the BBGS during the acceleration phase in early-2011.

2. The Bering-Bagley Glacier System: Geography and Surge History

2.1. BBGS Geography and Surge History

The BBGS, which extends from the Logan Massive in western Canada to southeastern Alaska near the Gulf of Alaska, is the largest temperate surge-type glacier system on Earth, and the largest and longest glacier in North America, with an area of approximately 5,175 km^2 and a length of over 190 km (for coordinate box, see Figure 1). The geography of the BBGS, sometimes referred to as simply the Bering Glacier System (BGS), is described in Molnia (2008) and in Molnia and Post (2010). A photographic documentation of the 1993 – 1995 surge is given in Herzfeld (1998).

Geographic features that are important landmarks during the progression of the surge are marked in Figure 1a. This figure also shows the model domain, defined to include the surging parts of the BBGS. The main Bering Glacier is a surge-type glacier (Post, 1969); the surge dynamics extends into the Eastern Bagley Ice Field, also named Bagley Ice Valley, as noted in 1995 (Herzfeld & Mayer, 1997) and observed again in 2011 – 2013 (Herzfeld, McDonald, Stachura, et al., 2013; Herzfeld, McDonald, & Weltman, 2013), while the Western Bagley Ice Field is not affected by the surge process. The neighboring Steller Glacier originates in the Western Bagley Ice Field and shares a medial moraine with the lobe of Bering Glacier. During a surge of Bering Glacier,

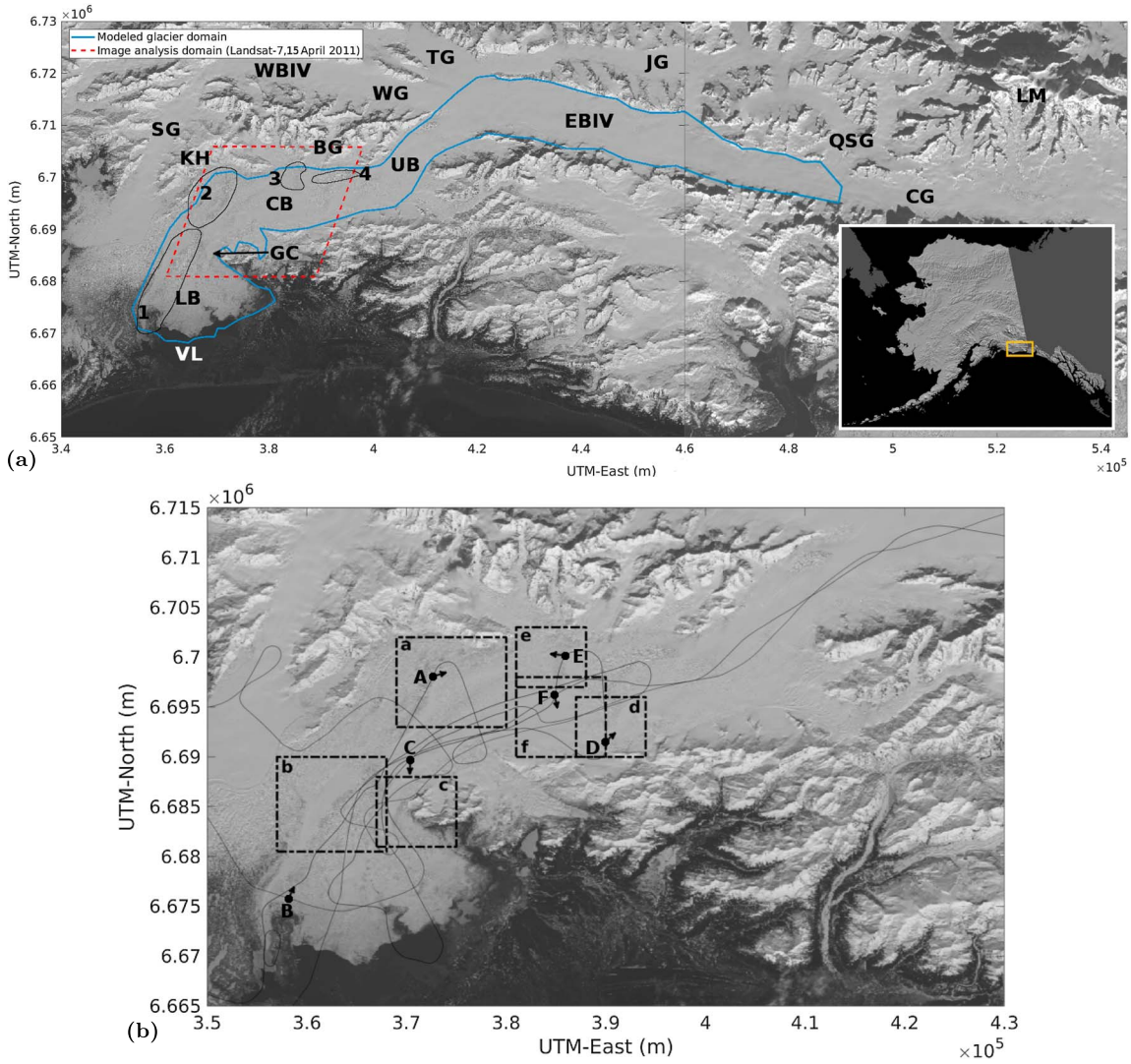

Figure 1. The Bering Bagley Glacier System with key locations and subdomains referenced throughout the paper. (a) The intersection of the image analysis domain (red dashed line) and the modeled glacier domain (solid blue line) is the domain of the model-data comparison analysis presented in this paper. Numbers refer to adjacent regions outlined by thin black lines: 1 = Tashalich Arm; 2 = Khitrov Crevasses; 3 = Betge Crevasses; 4 = Rift Area. LB = Lower Bering Glacier; CB = Central Bering Glacier; UB = Upper Bering Glacier; EBIV = Eastern Bagley Ice Valley; WBIV = Western Bagley Ice Valley; SG = Steller Glacier; BG = Betge Glacier; WG = Waxell Glacier; TG = Tana Glacier; JG = Jefferies Glacier; QSG = Quintino Sella Glacier; CG = Columbus Glacier; LM = Logan Massive; VL = Vitus Lake; GC = Grindle Corner; KH = Khitrov Hills. The Bering Bagley Glacier System is surrounded by the Chugach-Saint Elias mountain range. Background images from Landsat-8 acquired on 28 April 2013 (left) and 7 March 2014 (right). Reference image in lower right: U.S. Geological Survey Map I-2585. (b) Reference figure for aerial images in Figure 2 and crevasse orientation images in Figure 4. The thin black line traces the flight paths of the Fall 2011 airborne campaign over the Bering Bagley Glacier System. Black dots give the locations of the aerial images in Figure 2, labeled with corresponding capital letters (A)–(F). Emanating arrows give the camera pointing direction. Dashed black boxes trace the regions shown in Figure 4 and are labeled with corresponding lowercase letters (a)–(f). Background image from Landsat-8 acquired on 28 April 2013.

Steller Glacier has been observed to pulse, but not surge, a terminology first used by Austin Post (Molnia & Post, 2010; Post, 1969). (A pulse is an acceleration that is local in space and time and does not spread across the entire glacier.) In 1995, Steller Glacier pulsed significantly (Herzfeld & Mayer, 1997) but less so during the 2011–2013 surge according to our airborne observations. The BBGS also includes the nonsurging Quintino Sella Glacier near the Logan Massive in Canada and the Columbus Glacier. The confluence of these two glaciers marks the start of the upper Eastern Bagley Ice Field. Glaciers connected to the BBGS include the east flowing Waxell Glacier in the Western Bagley Ice Field, the Tana Glacier, a northern tributary which receives about half its ice flow from the Western Bagley Ice Field, and Jefferies Glacier, which is north of and connected to the BBGS via a single outlet glacier, but not a part of the BBGS as most of Jefferies Glacier drains to the north away from the BBGS.

Figure 2. Imagery from campaign flight over Bering Glacier 25 September 2011. (a) Kitrov crevasses, (b) Upper Tashalich Arm, (c) Upper Grindle Corner (looking down-glacier), (d) high roughness anomaly in central Bering with a supraglacial lake directly up-glacier, (e) extensional crevasse province near the confluence of Betge Glacier (Betge Crevasses), and (f) noncrevassed area in the center of Bering Glacier (foreground). Figure 1b provides locations along the flightpath where each image was taken along with their approximate look angles.

Bering Glacier terminates in a series of large proglacial lakes, the largest of which is Vitus Lake. The lakes are separated from the Gulf of Alaska by a ~200-m-wide spit that is segmented by the Seal River. Bering Glacier is grounded at the calving front where buoyant forces cause the calved ice to rise above the terminus height (Lingle et al., 1993). During a surge, the glacier advances into and over the proglacial lakes (Herzfeld, 1998; Molnia & Post, 1995; Molnia & Williams, 2001; Post, 1972; Turrin et al., 2013). As a result of the advance, the surge affects the ecological balance in the environment surrounding the glacier and potentially threatens shipping lanes through iceberg calving. Therefore, understanding the surge is important not only as a glaciological phenomenon but also for the environment and society.

Bering Glacier has been retreating from its Litte Ice Age maximum in the late 1800s interrupted by periodic surge events as indicated by characteristic folded medial moraines (Crossen & Lowell, 2010; Molnia & Post, 1995; Post, 1969). Early observations of a surge in 1938–1940 go back to R. M. Krimmel (USGS). Bering Glacier surged again in 1957–1967 (Molnia & Post, 2010; Post, 1972) and in 1993–1997 (Fatland & Lingle, 1998, 2002; Fleischer et al., 2010; Herzfeld, 1998; Herzfeld & Mayer, 1997; Josberger et al., 2010; Lingle et al., 1993; Mayer & Herzfeld, 2000; Molnia, 2008; Molnia & Post, 1995, 2010; Molnia & Williams, 2001; Roush et al., 2003; Shuchman & Josberger, 2010; Shuchman et al., 2010).

2.2. Summary of Processes of the Recent Surge

Bering Glacier started to surge in 2008 and stopped in the same year (Burgess et al., 2013; Turrin et al., 2013). No surge activity occurred in 2009–2010, as reflected in satellite imagery. In Spring 2011, Bering Glacier's dynamics changed to a full-scale surge resulting in crevassing throughout a large portion of the glacier (Herzfeld et al., 2013). The early-2011 acceleration resulted in significant surge crevassing mostly along the longitudinally northern branch (north of the center flowline) of the central and lower Bering Glacier, extending into Tashalich Arm, the westernmost part of the lobe (Herzfeld et al., 2013). We refer to this acceleration as the early-2011 phase of the BBGS surge. During the early-2011 surge phase, a bulge that had formed during quiescent phase collapsed, as determined by a 70-m elevation loss, and ice mass transferred down glacier along Tashalich Arm led to a 20- to 40-m surface height increase by Fall 2011 (Herzfeld et al., 2013). The bulge collapse resulted in the formation of large surge crevasses in the Khitrov crevasse field. Early surge dynamics also affected the Grindle Corner area (see Figure 1). Velocities for 2010 are derived from SAR data for Bering Glacier, and for 2011 for a small subarea of the glacier in Burgess et al. (2013). A similar study is conducted using Landsat-7 imagery and both automatic and manual feature tracking in Turrin et al. (2013). Our aerial observations in Fall 2012 and Fall 2013 revealed a new surge phase in 2012 that was characterized by fresh crevassing and drawdowns along the longitudinally southern branch of Bering Glacier. The surge continued to expand in 2013 to affect increasingly easterly locations in the Eastern Bagley Ice Field. No new surge deformations were observed in 2014.

Airborne imagery collected in our Fall 2011 campaign to the BBGS (Herzfeld et al., 2013) is given in Figure 2, which shows the locations that were most affected by the early-2011 phase of the surge. The flightpath for our Fall 2011 campaign is marked by the thin black line in Figure 1b. Additionally, Figure 1b displays black dots with arrows specifying locations and look angles of the aerial images in Figure 2.

3. Methods and Approach

3.1. Overview of Approach

The principal idea of our approach is to use crevassing as the central parameter in both modeling and data analysis, because crevassing is the most obvious manifestation of the rapid acceleration processes that are characteristic of a surge. Crevassing has sufficient spatial resolution and locally specific characteristics to function as a useful geophysical variable. Crevasse characteristics can be derived from both observational data analysis and numerical modeling. Therefore, we use crevasses as a means to compare numerical modeling and image-data analysis when investigating the surge phenomenon.

The work in this paper has three components: (1) data analysis, (2) numerical modeling, and (3) model-data comparison. More specifically, we proceed (1) to derive crevasse characteristics following the principles of structural glaciology carried out by calculation of parameterized roughness from geostatistical functions, (2) to numerically model material fracture of ice in rapid and complex motion, that is, crevasse formation, and (3) to employ quantitative and spatial model-data comparisons using three different mathematical measures.

Observations of crevasse fields stem from two sources: airborne imagery collected in flight campaigns during the surge (Figure 2), and satellite optical imagery from Landsat-7 (Figures 3a and 3b). Geostatistical characterization is applied to map and characterize crevasse fields from satellite image data. The geostatistical characterization proceeds by calculation of spatial functions, derivation of roughness parameters from those functions (especially the *pond* parameter for several directions, defined in section 4). A threshold is derived to classify crevassed regions and uncrevassed regions. On the modeling side, we set up a 3-D, full-Stokes, finite element model for the BBGS to simulate ice flow and glacier structure for a given time period. Simulation of the glacier's stress regime, together with a von Mises stress threshold, allows estimation of crevasse formation. Three crevasse-based model-data comparison methods are developed that compare crevasse location,

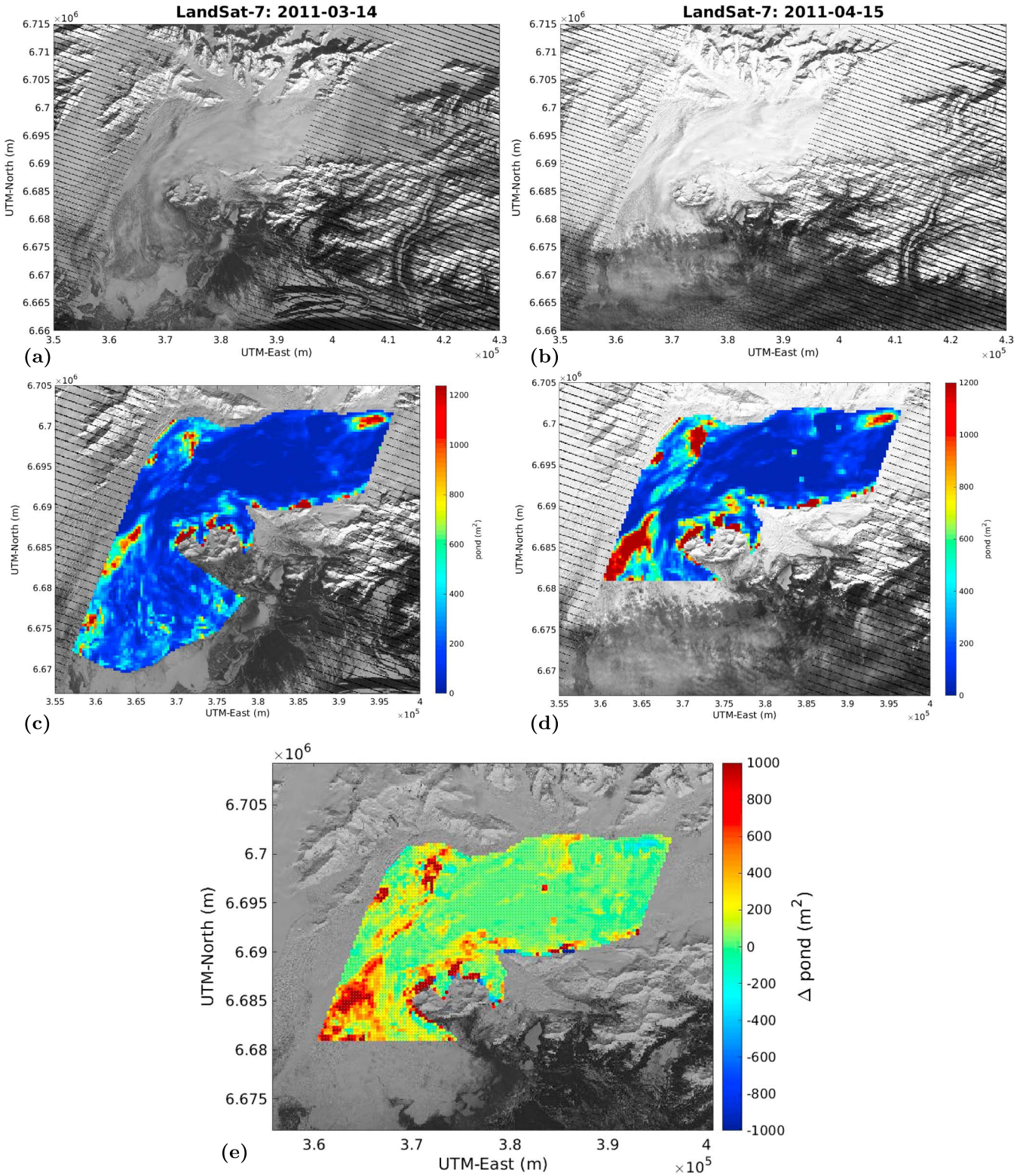

Figure 3. The mean *pond* spatial roughness measure (crevassity) and its change from 14 March 2011 to 15 April 2011, derived from Landsat-7 imagery. The *pond* value displayed here is the mean *pond* value over all 16 directional bins. (a) Landsat-7 panchromatic image from 14 March 2011 over Bering Glacier, Alaska. (b) Landsat-7 panchromatic image from 15 April 2011 with heavy cloud cover over the glacier lobe. (c and d) Mean *pond* value (over all 16 direction classes) applied to the images in (a) and (b), respectively. (e) Difference in the mean *pond* value from (c) to (d). A large positive change in the mean *pond* value (roughness; crevassity) indicates dynamic activity resulting in surface deformation. The background image for (e) is from Landsat-8 acquired on 28 April 2013.

orientation, and crevassity. The comparison methods allow evaluation of the model and estimation of unknown model parameters, thereby improving our understanding of the surge.

The work in this paper also has three levels on each side (modeling and data analysis): For modeling, level 1, the basic approach is the generation of a numerical model of the glacier system during the surge. This uses physical laws and data-derived constraints, such as ice surface height and subglacial bedrock surface height. Level 2 is the simulation of crevasses, where a von Mises criterion is applied as a threshold for crevassing. For data analysis, level 1 is constituted by the geostatistical characterization, which is based on satellite data. Level 2 is the mapping of crevasse existence and properties, using a threshold for a parameter. Level 3 brings together both data analysis and modeling in the application of metrics, which quantify similarity of level-2 results from both sides. We will conclude that both approaches are physically correct, where the metrics show good similarity, while regions of poor similarity will provide insights in the deficiencies that may have contributed to one of the components at one of the levels.

3.2. Relationship to Previous Work on Crevasse Analysis

Previous studies on crevassing have compared observed crevasses on a glacier's surface to the local stress regime of the ice. A common approach to investigate crevassing is to first derive surface strain rates, easily obtained from observed velocity gradients, through which the stress regime is estimated by inversion of a constitutive equation describing glacier flow such as Glen's Flow law. When investigating crevassing, strain rate fields have traditionally been derived using in situ measurements of ice displacement using a network of stakes that have been drilled into the surface (e.g., Harper et al., 1998; Holdsworth, 1969; Vaughan, 1993). Applications of such in situ methods for calculation of strain rates for the entire BBGS is not feasible because of the sheer size of the glacier system. In addition, the heavy crevassing, presence of water on and near the surface, and sudden surface changes during a surge, makes field work on the ground difficult, if not impossible. This calls for methods of remote sensing when studying a surge in a large and complex glacier system. Herzfeld and Zahner (2001) use a neural network to classify crevasse types from video imagery. Studies such as Clason et al. (2012) and Poinar et al. (2015) have used satellite remote sensing in the form of synthetic aperture radar or optical imagery to measure surface strain rates. However, as originally pointed out by Glen (1955), there can be high uncertainties in inverting strain rates to estimate stress due to unknown dependencies such as ice temperature. Moreover, the large deformation during a surge destroys surface features used in the correlation methods of satellite imagery (Massonnet & Feigl, 1998). This motivates our approach to studying crevasses using methods of numerical modeling and noncorrelation-based image analysis (independent of correlation) as summarized in the following.

3.3. Crevasse Characterization Based on Structural Glaciology and Geostatistics

Crevasse characterization using generalized surface roughness, combined with the principles of structural glaciology, is utilized as an approach to study surge processes in a large and complex system (see, e.g., Herzfeld & Mayer, 1997; Herzfeld et al., 2014; Mayer & Herzfeld, 2000). The principles of structural geology provide links between dynamics, kinematics, and deformation of the glacier, which can be formalized and quantified using continuum mechanics (Herzfeld et al., 2004, 2014; Herzfeld & Mayer, 1997; Liu, 2002; Mayer & Herzfeld, 2000; Means, 1976; Suppe, 1985; Twiss & Moore, 1992) and represented numerically in a model (Hubbard & Hubbard, 2000). The principles of continuum mechanics are introduced in Greve (2003) for ice dynamics and in Ramsay and Lisle (2000) for structural geology. The concept of generalized spatial surface roughness includes all morphological characteristics of the ice surface, which form in consequence of ice dynamic and environmental processes, such as precipitation and melting, and lead to metamorphosis of snow and ice, deformation, and transport. Our mathematical approach of analysis and parameterization of spatial surface roughness is described in Herzfeld (2008) and applied here to characterize crevasse types based on satellite imagery. The crevasse characterization is based on calculation of spatial statistical structure functions and a set of parameters derived from these functions. The mathematical roughness analysis, combined with the principles of structural glaciology, allows derivation of deformation characteristics in accelerating glaciers (see Herzfeld et al., 2004). This approach was employed in Herzfeld et al. (2014) in an analysis of the rapid surface lowering and retreat of the fast-moving Jakobshavn Isbræ using a single generalizing roughness parameter, and roughness analysis was found to contribute to an explanation of the processes causing retreat. In the present study, we use surface roughness derived from Landsat-7 optical imagery to identify crevassed regions by applying a threshold to a roughness parameter and using its magnitude to quantify crevassity, that is, the amount of ice-surface deformation.

3.4. Numerical Modeling of Crevasses

To better understand the mechanisms controlling the surge phenomenon, we develop a numerical model of the BBGS that has the ability to predict crevasse location and orientation along with estimates of crevassity, allowing direct comparisons to our geostatistical image analysis. Studies by Vaughan (1993) and Hubbard and Hubbard (2000) have shown the usefulness of glacier modeling in analyzing the structure of a glacier and its surface expressions. We set up a full-Stokes numerical model for the BBGS and solve the (quasi) steady state system for ice flow using the finite element software Elmer/Ice (Gagliardini et al., 2013). The modeling effort requires surface topography, subglacial topography, a flow law, and specific boundary conditions. Particular attention is given to the ice/bedrock interface as nearly all the ice movement during the surge is attributed to sliding at the glacier base, which for Alaskan surge glaciers is due to changes in the subglacial hydrological system (Cuffey & Paterson, 2010).

Given a modeled stress regime, a maximum stress criterion is adopted to predict where surface crevassing occurs. Such a criterion usually compares a measure of the principal surface stresses to some stress threshold corresponding to the yield strength of the ice. Vaughan (1993) analyzed several critical stress-fracture criteria including the von Mises criterion (Maximum octahedral shear stress), which we adopt in our analysis as the strength measure required for crevassing to occur in the surface plane of the glacier. The crevasse-based model-data comparisons introduced in section 6 provide a means for finding an optimal ice strength threshold value.

4. Crevasse Analysis From Observations

4.1. Geostatistical Characterization

The objective of a mathematical characterization is to derive a set of parameters that uniquely describe an object. Here the goal is to characterize the micromorphology, or spatial roughness, of the ice surface within a crevasse province. A crevasse province is an area that is homogeneous with respect to its spatial surface properties and that is maximal with respect to this homogeneity property. To capture the spatial characteristics of an ice surface province, we analyze generalized surface roughness using the following concepts, which are introduced in a mathematical and applied context in Herzfeld (2008).

The analysis is based on the *first-order vario function*, v_1, which is a spatial structure function defined as follows:

Let $\mathcal{D}$ be a region in $\mathbb{R}^3$ or $\mathbb{R}^2$ and z a random variable defined over $\mathcal{D}$. For pairs of points $(x_i, z(x_i)), (x_i+h, z(x_i+h)) \in \mathcal{D}$, let

$$v_1(h) = \frac{1}{2n}\sum_{i=1}^{n}[z(x_i) - z(x_i+h)]^2 \tag{1}$$

where n is the number of pairs separated by the lag vector h. The vario function is a discrete mathematics analog to the variogram of geostatistics. In practice, a vario function is calculated for measurements of the geophysical variable using discrete bins of lag (separation) distance (h). The lag bin width often corresponds to the resolution of the measurements from which the vario function is derived. Directional vario functions are calculated for lag vectors in directional bins or classes. It is common to calculate (directional) vario functions within a moving window, that is, for an along-track segment (1D) or within some rectangular subset of an image (2D). The window moves across the domain of interest according to a defined offset or spacing that relates to the resolution of the final geostatistical analysis. In this analysis, we calculate vario functions within a specified window size at each location on a grid whose resolution is similar to that of a numerical model.

From the vario function, geostatistical parameters are derived to characterize spatial structure. In this paper, we use only a single geostatistical parameter to characterize the ice surface: the *pond* parameter, defined as the maximum value of the vario function. The *pond* parameter describes the overall spatial roughness of the ice surface.

4.2. Method Applied to Landsat-7 Imagery

Surge crevasses can be distinguished in Landsat-7's Enhanced Thematic Mapper Plus (ETM+) panchromatic imagery at 15-m resolution. In Landsat-7 data, surface properties are captured by reflected energy and measured in units of absolute radiance at the sensor. In this analysis, we use the GeoTIFF data product, which scales measured radiance into a $[0, 255]$ grayscale interval. The random geophysical variable

is thus the surface property, radiance, and the realization, $z(x)$, is the measurement given in the Landsat-7 GeoTiff image. Therefore, we apply equation (1) to measured radiance values.

Landsat-7 panchromatic data are selected for analysis because the 15-m resolution allows identification of crevasses and one single image captures most of the BBGS. Throughout this analysis, we use two LandSat-7 images from early-2011. The first image was taken on 14 March 2011, while the second was taken 32 days later on 15 April 2011 (Figures 3a and 3b, respectively). Parts of these images contain clouds and/or striped artifacts, which restricts the study domain. (For information on the striped artifacts in Landsat-7 images see Markham et al., 2004). Fortunately, the cloud- and stripe-free regions in these images provide a study domain that coincides with the area of interest on the BBGS where most of the dynamic activity occurred during the 2011 phase of the surge. Within this study domain, we derive roughness characteristics using geostatistical methods.

Directional vario functions and characteristic parameters are calculated within subdomains (windows) centered at points on a 2-D grid that spans the study region. Here we use a 600-by-600 m grid (40-by-40 pixels) and a local window size of 600-by-600 m. Within each window, we calculate the *pond* parameter from directional variograms along 16 directional classes of 11.25° width. Crevasse presence is estimated at a given location if the mean value of *pond* over all directions exceeds an empirical threshold of $pond_{\text{thresh}} = 35\ \text{m}^2$. The direction-averaged *pond* value, or simply the mean *pond* value, is used as a measure of crevassity. As shown in Figures 3c and 3d, the mean *pond* value is much higher in areas of large and complex deformation, such as the Khitrov crevasse field, while much lower in areas of simple one-directional crevasses as in the Betge crevasse field (compare to Figure 2). Thus, the mean *pond* value consistently captures the magnitude and complexity of deformation at the ice surface, and we use it as a measure for crevassity. We note here that more sophisticated measures of crevassity may include additional geostatistical parameters derived from the vario function such as the *mindist* parameter, which relates to crevasse spacing, or the $p1$ parameter, which captures the significance of features and feature size (see Herzfeld, 2008).

4.3. Assigning Crevasse Orientation

Crevasse orientations are assigned manually at the locations where crevasses are determined to be present from the geostatistical analysis. Crevasse orientations are assigned one of 16 potential directions. In other words, the resolution of the direction analysis is $180/16 = 11.25°$. The normalized blue vectors in Figure 4 show the crevasse locations, determined from the mean *pond* threshold, and orientations, determined manually, for the Landsat-7 image taken on 15 April 2011. Subfigures (a)–(f) display crevasse existence and orientations for interesting regions throughout the glacier (compare each subfigure to corresponding aerial images in Figure 2). The subdomain of each subfigure is given by dashed-black boxes in Figure 1b with corresponding lowercase letters.

4.4. Determination of Recent Deformation

The change in the mean *pond* parameter can be used as a means to discriminate times when deformation occurred. However, in this analysis we assume that the mean *pond* parameter calculated for a single image represents recent ice deformation occurring in early-2011, as opposed to deformation occurring at some time previous. Fresh crevasses are identified within the study area for early-2011 by utilizing airborne data from our field observations in 2011 (sharp crevasse edges indicate newly opens crevasses), and also time series of satellite imagery. As such, we do not expect the observed crevasses in this area to have been transported from up-glacier. Possible exceptions include areas where crevasses are present in quiescent phase, such as the Khitrov Crevasses or the Grindle Corner, and the far up-glacier portion of the study area that was affected by the 2008 acceleration.

The change in the mean *pond* value between the 14 March 2011 image and the 15 April 2011 image is shown in Figure 3e. Note that this value has increased in the locations of large mean *pond* values as derived from in the 15 April 2011 image (Figure 3d). The only significant difference occurs in the area of a large rift (see Figure 1a for definition of rift area). The rift formed in the winter of 2008–2009 as determined from Landsat imagery, and therefore, not much emphasis is placed on interpreting this area for this analysis. Therefore, we use geostatistical characterizations of the 15 April 2011 image to represent the recent surface deformation that occurred during the early-2011 surge phase. Change in mean *pond* is likely needed when applying this method to time periods following the onset of the major surge phase, in particular, when comparing to longer transient model simulations that analyze surface structure evolution.

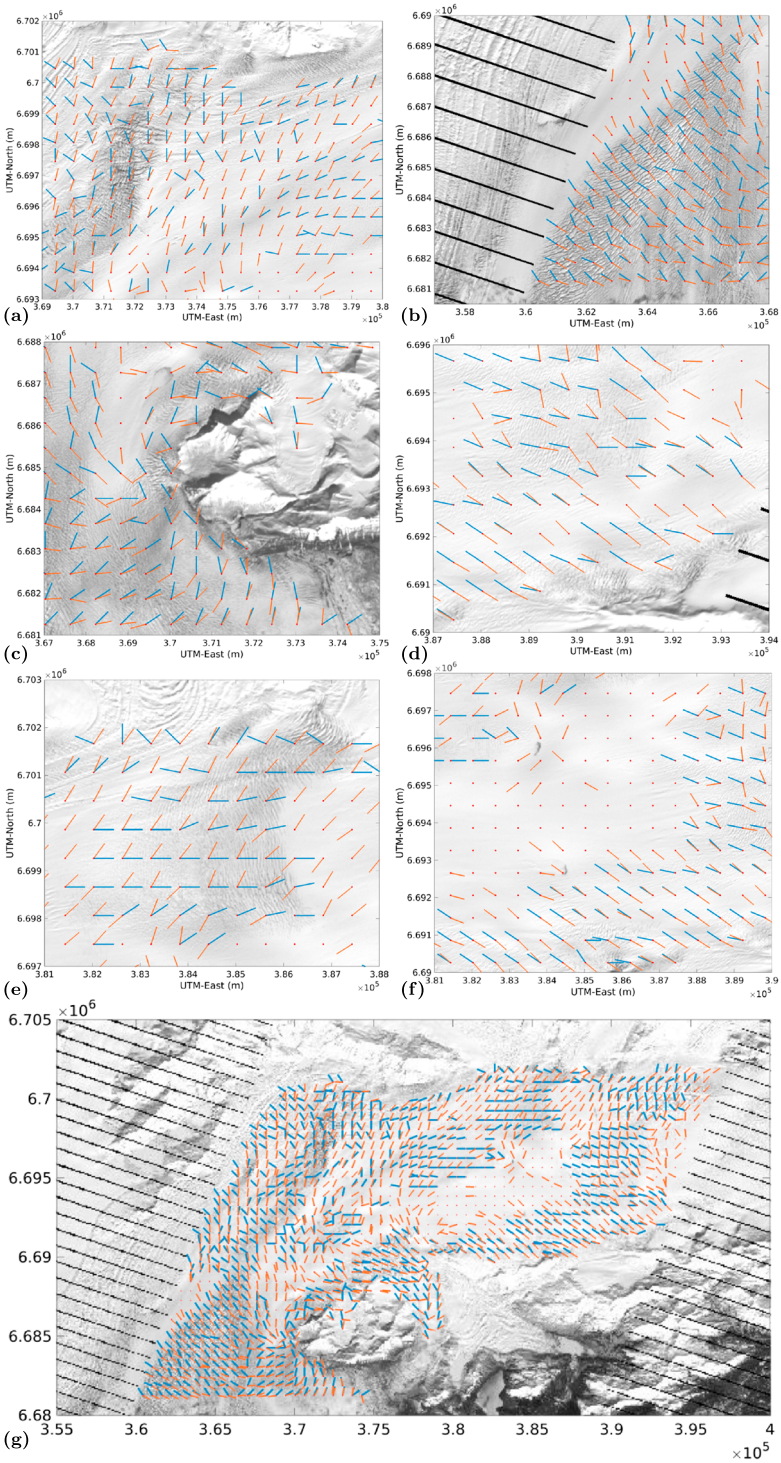

Figure 4. Orientations of dominant surface crevasses on the Bering Bagley Glacier System derived from Landsat-7 images taken on 15 April 2011 (blue) and from the numerical model (orange). Lines are oriented normal to the crevasses (or dominant surface feature) within each 600-by-600 m window. Red dots give the nodal location where crevasse characteristics are estimates (i.e., the window center). (a) Khitrov crevasses, (b) Tashalich Arm, (c)Grindle Corner, (d) southern branch of Bering glacier, (e) Betge crevasses, and (f) central Bering Glacier. Figure 1b provides reference locations on the Bering Bagley Glacier System for subplots (a)–(f) in this figure. (g) Crevasse orientations for the entire study area. Background image: LandSat-7 panchromatic taken 15 April 2011. Black stripes are a result of a malfunctioning of the Landsat-7 sensor.

5. Crevasse Analysis From Modeling

5.1. Model Description

To model glacier flow of the BBGS during surge, we employ a full-Stokes three-dimensional model in order to analyze the full stress regime. Ice rheology is defined by Glen's Flow law together with an isothermal assumption for a temperate ice mass. Ice temperature is set to be a uniform and constant 0°C. The model is forced by gravity only. Additional forcings such as accumulation and ablation (surface mass balance) or hydrological changes are not necessary for the short time scale simulations we run here.

Flow and stress regime solutions are found using the open-source finite element software Elmer/Ice. A full description of the capabilities of Elmer/Ice can be found in Gagliardini et al. (2013). Results depend on the equations for ice flow, input geometry, and boundary conditions. Using these results, we utilize a crevasse criterion to simulate surface crevassing. We give a brief overview of the important aspects of the model followed by our approach to simulating crevasses.

5.1.1. Governing Equations for Ice Flow

Conservation of momentum and conservation of mass give respectively the governing force equilibrium and kinematic equations for Stokes flow:

$$\nabla \cdot \boldsymbol{\sigma} + \rho \boldsymbol{g} = \nabla \cdot (\boldsymbol{\tau} - p\,\boldsymbol{I}) + \rho \boldsymbol{g} = 0, \tag{2}$$

$$\nabla \cdot \boldsymbol{u} = tr(\dot{\boldsymbol{\epsilon}}) = 0, \tag{3}$$

where $\boldsymbol{\sigma} = \boldsymbol{\tau} - p\boldsymbol{I}$ is the Cauchy stress tensor, $\boldsymbol{\tau}$ the deviatoric stress tensor, p the pressure, ρ the ice density, $\boldsymbol{g} = (0, 0, -9.81)$ the gravity vector, $\boldsymbol{u}$ the velocity vector and $\dot{\boldsymbol{\epsilon}} = \frac{1}{2}(\nabla \boldsymbol{u} + (\nabla \boldsymbol{u})^T)$ the strain rate tensor, which is equivalent to the symmetric part of the velocity gradient.

Glacier creep is related to stress using the constitutive equation given by Glen's Flow law,

$$\boldsymbol{\tau} = 2\eta \dot{\boldsymbol{\epsilon}}, \tag{4}$$

where η is the effective viscosity defined as,

$$\eta = \frac{1}{2} A^{-1/n} \dot{\epsilon}_e^{(1-n)/n} \tag{5}$$

where $A = A(T)$ is a rheological parameter that depends on the ice temperature, T, via an Arrhenius law and $\dot{\epsilon}_e$ is the second invariant of the strain rate tensor termed the *effective strain rate*. The Glen exponent was taken to be $n = 3$, which is a well-established value for temperate glacier flow (Cuffey & Paterson, 2010).

5.1.2. Model Geometry, Meshing, and Simulation Characteristics

The model uses triangular elements with side lengths of 400 m in a 2-D footprint of the glacier which is then extruded to yield 5 vertical levels resulting in a 3-D representation. The bottom level matches the input bed topography and the upper-level matches the input surface topography. Vertical levels range in thickness from 2 to 300 m depending on location. Nodes along the perimeter of each 2-D layer define the lateral boundary of the 3-D glacier. The modeled glacier domain, or footprint, is given as a solid blue line in Figure 1a.

To define the glacier surface, an input Digital Elevation Model (DEM) of the BBGS is needed. We derive the DEM from CryoSat-2 Synthetic Aperture Interferometric Radar Altimeter (SIRAL) data using Advanced Ordinary Kriging as described in Trantow and Herzfeld (2016, Figure 5a). For analysis in the present paper, SIRAL Level-2 Baseline-C data (Bouffard, 2015), measured between November 2010 and April 2011, are processed for the entire BBGS. Baseline-C data in the Bering Glacier region require the addition of 59.959 m of elevation to each data point due to a systematic error in the Level-2 processing. This error has been identified and corrected by the authors when deriving the DEM used in this study and will be corrected in future data releases from European Space Agency (ESA) (personal communication with Steven Baker [University College London], Veit Helm [Alfred Wegener Institute], Johan Nilsson [Jet Propulsion Laboratory], Mark Drinkwater, Tommaso Parrinello, and Jerome Bouffard [all ESA] at the North American CryoSat-2 Meeting, March 2017). We derive a DEM using the advanced ordinary kriging method for input bedrock topography using measurements made by NASA's Jet Propulsion Laboratory who deployed an ice penetrating radar system called the Wide-field Infrared Survey Explorer (WISE) in 2008 and 2012 over the BBGS (Figure 5b; Rignol et al., 2013).

We are interested in the stress regime of the BBGS ice surface at a given time in early-2011, and thus a quasi steady state simulation is run. For our purposes, a quasi steady state simulation consists of running the model

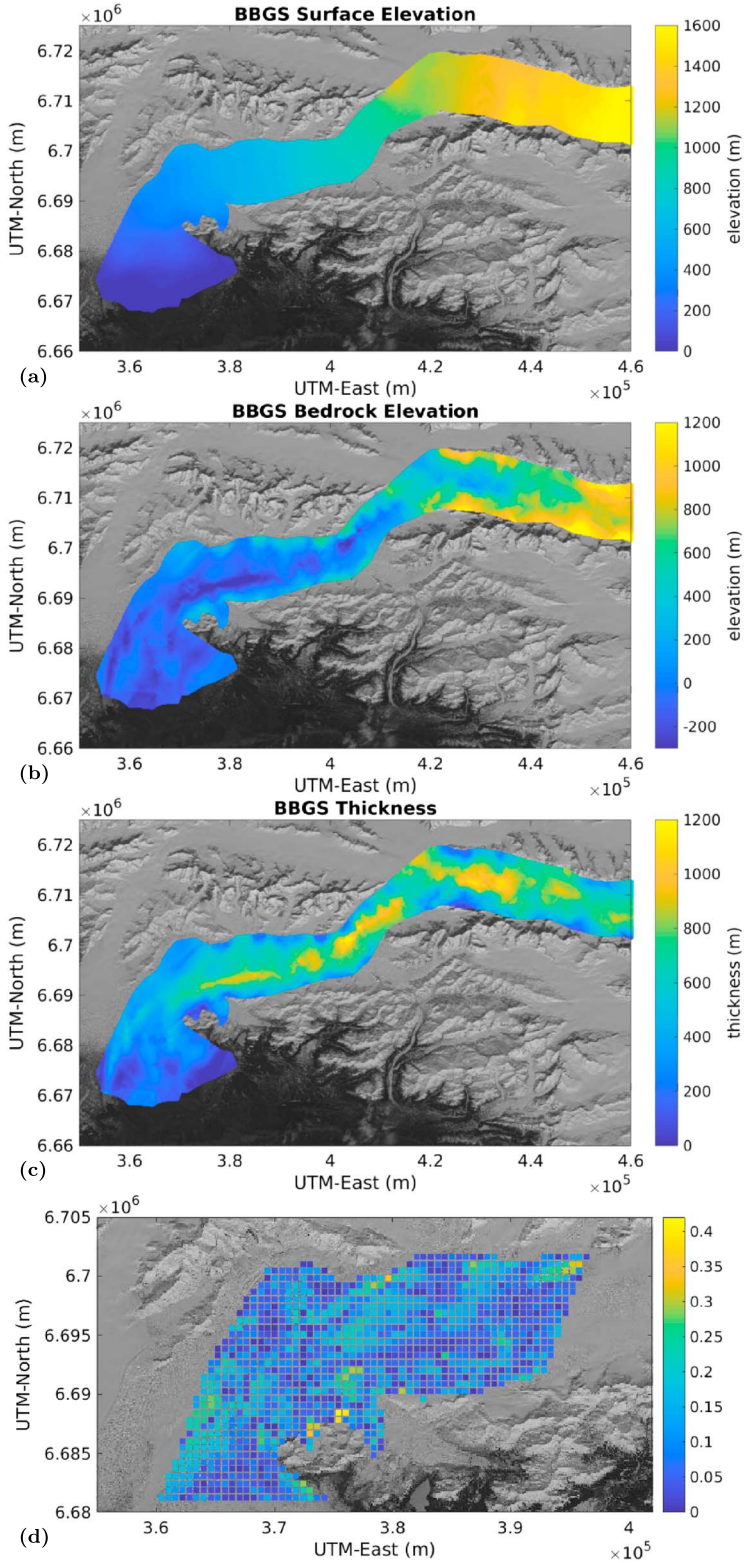

Figure 5. Bering Bagley Glacier System (BBGS) input model geometry and its relation to observed surface roughness. (a) BBGS surface topography derived from CryoSat-2 measurements. (b) BBGS bedrock topography derived from the Jet Propulsion Laboratory's Wide-field Infrared Survey Explorer (WISE) measurements. (c) Ice thickness in western BBGS in early-2011. (d) Map comparison between maps of the natural logarithm of the mean *pond* value (derived from a Landsat-7 image taken on 15 April 2011) and ice thickness as shown in (a).

forward for 20 iterations at 1-day time steps in order to reduce the influence of unrealistic effects that can result from errors in the input surface geometry (Zwinger & Moore, 2009), while overall still retaining the appropriate geometrical representation of the time period of investigation.

5.1.3. Boundary Conditions

Particular attention is given to the ice/bedrock interface as nearly all the ice movement during the surge is attributed to sliding at the glacier base, which for Alaskan surge glaciers is connected to changes in the subglacial hydrological system (Cuffey & Paterson, 2010; Kamb et al., 1985). Conditions for the ice/bedrock boundary allow no normal flux, and a linear friction law is employed,

$$\sigma_{nt} = \beta u_t, \tag{6}$$

where σ_{nt} is the basal shear stresses and u_t the tangential basal velocities (Gagliardini et al., 2013). The constant β is the linear basal friction coefficient, which is a parameter that can be tuned to match observations. The value of a basal friction coefficient for some sliding law is commonly found by inverting observed surface velocities (e.g., MacAyeal, 1992; Morlighem et al., 2010; Seroussi et al., 2011) using data sets with sufficient spatial coverage. However, this standard approach does not work well in a surging environment, where ice velocity is poorly constrained using feature tracking techniques. Alternatively, application of the crevasse analysis approach allows to optimize the basal friction parameter (see section 7). An optimized value of $\beta = 10^{-5}\,\frac{MPa \cdot a}{m}$ is used here.

The ice/atmosphere boundary at the upper surface is represented by a stress-free boundary. At the lateral boundaries, normal velocities are set to zero and tangential velocities are constrained by a linear sliding law similar to that at the base of the glacier. The lateral boundaries are treated uniformly throughout the entire glacier perimeter. This implementation effectively represents regions constrained by rigid mountains but does not necessarily represent behavior at the glacier terminus. This is not a severe restriction since the study region of this paper is over 10 km away from the terminus. From the experiments run in Trantow (2014), we find empirically that modeled velocities near and at the lateral margins are consistent with observations when assigning the lateral friction coefficient (β_{lat}) to be 1–2 orders of magnitude larger than the basal friction coefficient. For the present analysis, we set the value of β_{lat} to be 50 times that of β in the basal friction law, that is, $\beta_{\text{lat}} = 5\times10^{-4}\,\frac{MPa \cdot a}{m}$. Note that while we do not attempt to optimize β_{lat} in this study, it may be included as an unknown parameter and optimized in the same way as its basal counterpart (see section 7).

5.2. Criteria for Crevasse Formation: The von Mises Condition

The Cauchy stress tensor ($\boldsymbol{\sigma}$) is obtained from the flow solution in equation (2). In three dimensions, the state of stress at some point is fully described by six independent components of the symmetric tensor,

$$\boldsymbol{\sigma} = \begin{pmatrix} \sigma_{xx} & \sigma_{xy} & \sigma_{xz} \\ \sigma_{yx} & \sigma_{yy} & \sigma_{yz} \\ \sigma_{zx} & \sigma_{zy} & \sigma_{zz} \end{pmatrix} \tag{7}$$

where $\sigma_{ij} = \sigma_{ji}$, $i, j = x, y, z$. The diagonal elements, called the *normal stresses*, describe extensional ($\sigma_{ii} > 0$) or compressional ($\sigma_{ii} < 0$) stress along the Cartesian axes. The off-diagonal elements are the *shear stresses*, sometimes labeled $\sigma_{ij} = \tau_{ij}$ with $i \neq j$, acting normal to the i plane and in the j direction.

The *principal stresses* are given by the eigenvalues of the Cauchy stress tensor where principal directions (or axes) are given by the respective eigenvectors. The principal stresses are independent of the coordinate system and the state of stress at any point can be represented by a diagonal matrix with the principal stresses as the diagonal elements. This is achieved through a rigid transformation using an orthogonal matrix U so that

$$\boldsymbol{\sigma} = \begin{pmatrix} \sigma_{xx} & \sigma_{xy} & \sigma_{xz} \\ \sigma_{yx} & \sigma_{yy} & \sigma_{yz} \\ \sigma_{zx} & \sigma_{zy} & \sigma_{zz} \end{pmatrix} = U^T \begin{pmatrix} \sigma_1 & 0 & 0 \\ 0 & \sigma_2 & 0 \\ 0 & 0 & \sigma_3 \end{pmatrix} U \tag{8}$$

with $\sigma_1 \geq \sigma_2 \geq \sigma_3$ where, if positive, σ_1 represents the *maximum tensile stress* that the element experiences.

Crevasses will form once critical conditions of local stress are reached, implying that once some ice strength threshold (or yield stress) is exceeded, macroscopic deformation will occur, that is, *crevassing* (Kehle, 1964; Vaughan, 1993). Yet the range of threshold values can be quite large due to the many factors that affect crevasse formation. These factors include, but are not limited to, ice temperature, bulk physical properties of the ice, or firn, such as the density or amount of debris, and interactions at the ice/bedrock interface

(Holdsworth, 1965). Vaughan (1993) gave a stress threshold range of 90–320 kPa for crevasses to open in cold and temperate glaciers, while later studies by Forster et al. (1999) refined this range to 169–224 kPa for temperate glaciers.

At the upper free surface of the glacier, it is assumed that no normal force or traction exists, implying that one of the principal stresses is normal to the surface and equal to zero. The remaining two principal stresses are in the surface plane and control crevasse formation. These are given by σ_{1surf} and σ_{2surf}, where $\sigma_{1surf} \geq \sigma_{2surf}$.

Vaughan (1993) and later Forster et al. (1999) combine σ_{1surf} and σ_{2surf} following the von Mises and Griffiths criteria, along with the Coulomb criterion and the Maximum strain-energy dissipation criterion in the case of Vaughan, to determine an ideal stress measure for use in a failure criterion. For our study we used the von Mises criterion,

$$\sigma_{vm} = \sigma_{1surf}^2 + \sigma_{2surf}^2 - \sigma_{1surf} \cdot \sigma_{2surf} > \sigma_{threshold}, \tag{9}$$

to determine whether crevassing has occurred by checking if the von Mises stress measure (σ_{vm}) exceeds the given ice strength threshold ($\sigma_{threshold}$). We use a value of $\sigma_{threshold} = 200$ kPa, which is a result of a series of optimization steps as described in section 7.

5.3. Modeling Crevasse Orientation

To model crevasse orientation on the glacier surface, we assume that crevasses open perpendicular to the axis of maximal tensile stress (σ_1) at locations where the von Mises measure exceeded the prescribed stress threshold. With this formulation, we assume that crevasses are formed by tensile forces (Mode I fracturing in Van der Veen (1998, 1999)). Extensional crevasses are thought to open perpendicular to the axis of maximal tensile stress when assuming a singular mode of fracture through extensional opening. However, there have been observed discrepancies between the orientation of crevasses and the local axis of principal tensile stress explained by either rotations through advection of the crevasse through the velocity field or by a mixed-mode fracture involving compression or shear (Van der Veen, 1999). A failure criterion involving multiple principal stresses inherently accounts for mixed-mode fracture; however, the orientation of the fracture based on the combination of principal stresses remains unclear. As mentioned previously, we have identified that the crevasses within the study domain, with a possible exception of crevasses near the rift area, are newly formed as of early-2011. Therefore, we do not expect large deviations in orientation comparisons due to advection of previously formed crevasses. Rather, the differences in observed and modeled crevasses orientations are from either the occurrence of mixed-mode fracturing or from inaccuracies in the numerical model. The modeled axis of maximum principle stress is given as a normalized vector field in orange in Figure 4.

6. Model-Data Comparisons

6.1. Three Crevasse-Based Evaluation Methods for Model-Data Comparisons

To compare modeled crevasse fields to those observed in satellite imagery, three methods of model-data comparison are introduced:

Method 1: *A binary pointwise comparison of crevasse locations.* To evaluate crevasse existence at a given location throughout the glacier, we employ a binary yes/no approach, that is: Is crevassing estimated at a given location in both the data analysis and the model? At each nodal location within the study domain, we check whether crevassing is determined by the model via the von Mises stress condition, and/or in the image analysis via the mean *pond* parameter threshold.

Method 2: *A pointwise comparison between crevasse orientation vectors.* We evaluate crevasse orientation by calculating the angle, θ, between observed crevasse orientation vectors ($\vec{v}^{\,obs} = (v_1^{obs}, v_2^{obs})$) and the modeled axis of maximum principal stress ($\vec{v}^{\,mod} = (v_1^{mod}, v_2^{mod})$) for each location of crevasse existence agreement given by method 1. Derived model and observational orientation vectors are given at unit length.

Method 3: *Comparison of crevassity using similarity mapping.* A spatial analysis of the magnitudes of the data-derived mean *pond* value (surface roughness) and the model-derived von Mises stress value (σ_{vm}) is used to investigate the applicability of crevassity comparisons, motivated by the observation that larger values of each of these measures correspond to larger surface deformation at a given location. To make this comparison, we employ the Map Comparison method (MAPCOMP)

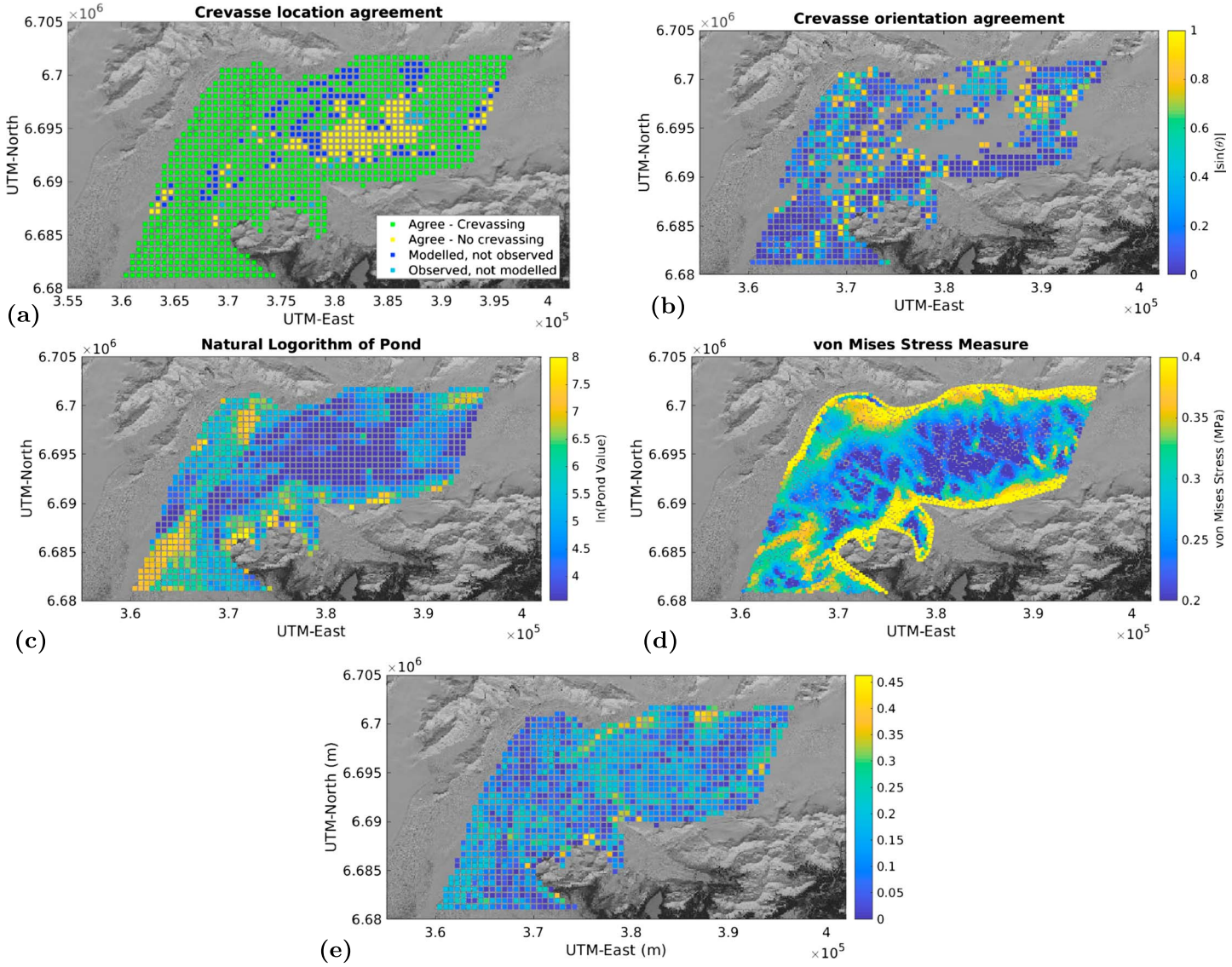

Figure 6. Results of the model-data comparisons. (a) Comparison of crevassed locations: Green points give locations where the model and observations agree there is crevassing, yellow points show agreement on noncrevassed regions, dark blue points give areas where modeled crevasses are predicted but are not seen in the imagery (using geostatistical methods) and light blue points are where crevasses were observed but not modeled. (b) Comparison of crevasse orientations: The absolute value of the sine of the angle between modeled maximal principal stress axes and the observed crevasse orientation as identified manually in the Landsat-7 imagery. (c) The natural logarithm of the mean *pond* value from image analysis where *pond* > 35 m^2. (d) The modeled von Mises stress measure that exceeds $\sigma_{thresh} = 200$ kPa (at the model resolution). Maps (c) and (d) are scaled such that the lower bound corresponds to the respective threshold values used to determine crevasse locations. (e) MAPCOMP comparison between the natural logarithm of the mean *pond* value (subplot (c)) and the von Mises stress (subplot (d)). In general, lower values correspond to better agreement between the two maps.

introduced in Herzfeld and Merriam (1990). The MAPCOMP operator utilizes a distance measure based on an algebraic seminorm evaluated for each location of the study region and yields a map of similarities and dissimilarities among any number of input variables, where low values indicate high similarity among the input maps (input variables). Prior to the comparison, values for variables are standardized using a linear transformation into the range of values encountered in the respective image analysis and numerical modeling, excluding values exceeding the 95% quantile to account for outlier effects.

Since the grid structure of the model and the image analysis are different, we map variable estimates from the model's finite element grid to the 600-by-600 m image analysis grid. The mapping processes uses

an interpolation scheme based on neighboring points weighted by distance. The total amount of grid nodes within our study area in the image-analysis grid, that is, the model-data comparison grid, is $N = 1{,}185$.

6.2. Comparison Results

A spatial map that visualizes optimized model-data agreement with respect to crevasse location is given in Figure 6a (method 1 result). At a certain location, if both the von Mises stress threshold and the mean *pond* threshold are exceeded, then both methods agree that crevassing is present and a green colored dot is given there. Similarly, if neither of these measures exceed their respective thresholds, a yellow color is displayed at the nodal location indicating the model and image analysis agree that no crevassing has occurred. Locations where the model predicted crevassing but not the image analysis are given a dark blue color, and locations of light blue reflect the opposite case. This map displays 87.85% agreement in crevasse locations.

A map of the optimized crevasse orientation comparison is shown in Figure 6b (method 2 result). Areas of dark blue show modeled orientations in the same bin as those observed ($\theta \leq 11.25°$), while areas of green and yellow show disagreement of at least three bins ($\theta > 33.75°$). The number of nodal locations where crevasses exist as agreed upon by both the model and observations is $N_{\text{crev}} = 928$.

The result of map comparison applied to the natural logarithm of the mean *pond* value (Figure 6c) and the von Mises stress measure using the model run with optimized parameters (Figure 6d) is shown in Figure 6e (method 3 result). Low similarity values, given in blue, correspond to locations where the mean *pond* value and von Mises stress measures agree, while locations with higher values (yellow) reflect dissimilarity. The similarity map in Figure 6e shows that in general, there is similarity in the locations of high von Mises stress and high surface roughness and vice versa. Therefore, to expand on method 1 of model-data comparison of crevasse location, in particular at locations where crevasse existence is agreed upon by the model and data (green in Figure 6a), we can directly compare the von Mises stress and the logarithm of the direction-averaged *pond* (mean *pond*) value to infer information on the magnitude and complexity of surface deformation and its implication in the surge process. That is, we can use both these measures as monotonically increasing indicators of crevassity on the glacier surface.

7. Optimizing Unknown Model Parameters

7.1. Optimization Procedure

Next, we demonstrate how the crevasse-based approach can be applied to optimize two model parameters simultaneously. Optimal values for the ice strength threshold $\sigma_{\text{threshold}}$ (equation (9)) and the linear basal friction parameter β (equation (6)) are estimated by minimizing the differences in the crevassed-based model-data comparisons. We note that the optimized values determined in this section were used in the modeling results given in section 5. The overall model-data agreement is measured by introducing scalar measures α_1 and α_2 for method 1 (comparison of crevasse locations) and method 2 (comparison of crevasse orientation), respectively. For method 1, we define α_1 as the fraction of nodal locations where model and data observations disagree on crevasse existence,

$$\alpha_1 = \frac{N_{\text{disagree}}}{N} \quad \in \ [0, 1] \tag{10}$$

where N the total amount of nodal locations within our study domain and N_{disagree} are the nodal locations where model and observed crevasse disagree on crevasse existence.

The scalar measure for method 2 (α_2) is given by

$$\alpha_2 = \frac{\sum_{i=1}^{N_{\text{crev}}} |\sin(\theta)|}{N_{\text{crev}}} \quad \in \ [0, 1] \tag{11}$$

where θ is the angle between the model- and data-derived orientation (unit) vectors, $\vec{v}^{\,\text{obs}}$ and $\vec{v}^{\,\text{mod}}$ respectively, and N_{crev} is the number of nodal locations where crevasses are agreed to exist.

We minimize both measures to achieve the best model-data agreement by varying the unknown model parameters within respective ranges. The minimization is carried out using a simple cost function C given by

$$C(\alpha_1, \alpha_2) = w_1 \cdot \alpha_1 + w_2 \cdot \alpha_2 \tag{12}$$

where w_1 and w_2 are weighting functions for α_1 and α_2, respectively. In this analysis, we place much greater weight on the minimization of α_1, and not α_2, due to uncertainties in determination of crevasse orientation, which arises from possible mixed-mode fracturing and the presence of complex, multidirectional crevassing that occurs in several locations (e.g., Khitrov Crevasses and the lobe area). Therefore, we set $w_1 = 4$ and $w_2 = 1$.

In this study, we solve for global and uniform values for β and $\sigma_{\text{threshold}}$ as the simplest method for determining basal sliding and ice yield strength during a surge phase. A spatially variable approach could use a more advanced cost function that minimizes observed and modeled crevasse differences to estimate β and $\sigma_{\text{threshold}}$ at each nodal location given some regularization, such as those used in velocity-based approaches (e.g., Larour et al., 2014).

We run model simulations that vary the ice strength threshold $\sigma_{\text{threshold}}$ between 90 and 320 kPa (Vaughan, 1993) at increments of 5 kPa, and the basal friction parameter β between $10^{-4}\,\frac{MPa \cdot a}{m}$ and $10^{-6}\,\frac{MPa \cdot a}{m}$ incrementing the value of exponential by 0.25. The range of the basal friction parameter is determined empirically after running over 100 numerical experiments of our BBGS model in Trantow (2014). The lower bound on β corresponds to model simulations displaying quiescent speeds, where observed quiescent speeds for the BBGS are given by Fatland and Lingle (2002) and Turrin et al. (2013). The upper bound results in modeled velocities over 1,000 times that of quiescence, which well exceeds the maximum observed velocities during a BBGS surge (Herzfeld, 1998).

To fully capture the surge mechanism, implementation of an inversion routine to estimate the basal friction parameter, dependent on location, would be desirable. However, given the complexity of the surge of the BBGS and the relatively poor data control with respect to bed topography, surface velocity, and surface properties, we found that inversion was not feasible. Instead, we assume a linear sliding law with a spatially uniform sliding parameter (β). To best constrain the experiment, the discretized optimization was carried out, running a forward model experiment with a combination of β and $\sigma_{\text{threshold}}$ over any possible 2-D combination in a large range of values resulting in a total of 423 cases: 9 possible β values and 47 possible σ_{thresh} values.

7.2. Optimized Model Parameters

The agreement measures are minimized at $\alpha_1 = 0.1215$ and $\alpha_2 = 0.5405$ when the basal friction parameter for the linear sliding law is $\beta = 10^{-5}\,\frac{MPa \cdot a}{m}$ and the stress threshold is $\sigma_{\text{thresh}} = 200$ kPa. This optimized stress threshold falls in the range given by Forster et al. (1999) for crevassing in temperate glaciers.

For a fixed β value, prescribing threshold values lower than 200 kPa tend to match more observed crevasse locations but also models crevassing where no crevasses are observed, mostly in up-glacier regions of the study area. Increasing the threshold better matches noncrevassed locations but yields more areas of observed crevassing that are not matched by the model, mostly in areas down-glacier in the study region. Similarly, for a fixed $\sigma_{\text{threshold}}$ value, a lower β value will result in higher sliding velocities and larger surface stresses leading to more crevassing throughout the glacier, while a higher value serves to reduce overall surface crevassing.

The optimized value for the critical von Mises stress may not necessarily correspond to the threshold for which brittle failure in the ice occurs and a crevasse is initialized as described in Van der Veen (1999). Rather, this threshold value corresponds to deformation that results in crevasses that are large enough to be captured at the Landsat-7 panchromatic image resolution (15 m). For example, the small-scale features in the foreground of the aerial image in Figure 2f would not be considered an area of crevassing given by our threshold value whereas the large crevasses in each of the other images in Figure 2 are considered crevassed regions and are locations where the modeled von Mises stress exceeded the threshold.

7.3. Velocity Comparison

Independent evaluation of the optimized model parameters is given by the observed surface velocity we derived for Bering Glacier using Spring 2011 Landsat-7 data (Figure 7a). Surface velocity estimates are found by correlating the pair of LandSat-7 images described in section 4.2 using the Image Georectification and Feature Tracking Toolbox (ImGRAFT) (Messerli & Grinsted, 2015). ImGRAFT is an open-source software that applies cross-correlation methods to image features within a specific template size (or window). We use a window size of both 5-pixels-by-5-pixels (or 75 m-by-75 m) and 30-pixels-by-30-pixels (or 450 m-by-450 m) with each yielding similar estimates. Only estimates that have a sufficiently high signal-to-noise ratio are retained (SNR > 3.5). The modeled surface velocity, given our optimized parameters, is shown in Figure 7b, and the difference between observed and modeled velocity is shown in Figure 7c. The average and standard deviation

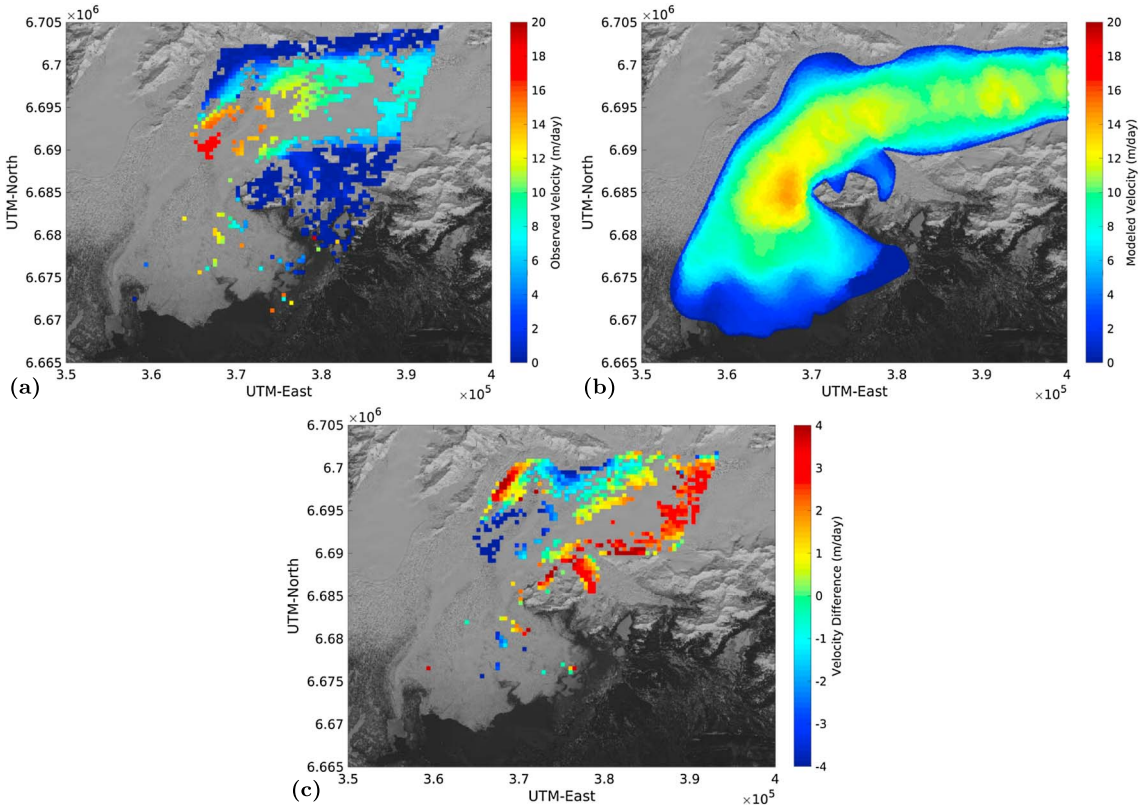

Figure 7. Surface velocity during the early-2011 phase of the surge. (a) Observed velocity derived from image correlation between two LandSat-7 photos taken 14 March 2011 and 15 April 2011. Only velocities with a signal-to-noise ratio higher than 3.5 are displayed. (b) Modeled velocity given a basal friction coefficient of $\beta = 1.0^{-5}$. (c) The difference in velocity (modeled minus observed). The average and standard deviation of the velocity difference is 0.54 ± 2.57 m/day.

of the nodal velocity difference is 0.54 ± 2.57 m/day. Modeled velocities are slightly overestimated up-glacier and underestimated down-glacier. However, with a uniform basal friction coefficient derived independently of observed velocity, the model reproduces the sparse observed data with similar longitudinal spatial patterns at correct magnitudes.

We note that our velocity estimates are spatially sparse due to decorrelation between the two images. This decorrelation arises from rapidly changing surface features associated with a surge and is a main reason to create an approach that does not rely on correlation of observations separated in time. The large gaps in observed velocity across our study domain, as seen in Figure 7a, prevents the application of velocity-based inverse methods for estimating the basal friction coefficient.

8. Effects of Bedrock Topography on Surface Crevassing

As observed in Herzfeld and Mayer (1997), Herzfeld (1998), and (Herzfeld et al., 2013), the first visible surface expression of the surge's kinematic wave is an occurrence of bidirectional crevasses with sharp edges in regions of high surface slope, indicative of bedrock slope. The reason is that the kinematic force of the surge breaks first at preexisting weaknesses caused by already crevassed ice or over relatively thin ice. Later, crevasse fields form without any connection to bedrock features, for example, the Betge Crevasses (see Figures 1a, 2e, and 4e).

In our analysis, we find that areas with the largest surface roughness and largest von Mises stress, away from the margin, correspond to locations of low glacier thickness near large gradients in the bedrock topography (see Figure 5c). In particular, we observe the largest surface roughness at the location where the main trough that exists in Central Bering Glacier splits into two trough branches that continue in the upper lobe area. A large angular crevasse field is observed at the location of this split (Figures 2b and 4b), mainly over the region between the two troughs where ice is shallower relative to the deeper troughs (see Figure 5). This crevasse field

is found in both data-derived and model-derived maps (Figures 6c and 6d). The eastern edge of the Khitrov crevasse field is traced by the gradient of bedrock height between the main trough of Central Bering Glacier and the raised bedrock south of the Khitrov Hills. This is the first location where surge crevasses occurred in 2011 and in 1993 (Herzfeld, 1998). There are also a few high-stress anomalies in Central Bering Glacier with correspondingly high roughness, such the one located at 390000 UTM-East/6694000 UTM-North shown in Figures 2d and 4d, which are associated with raised bedrock features. Each of these locations corresponds to significant bedrock gradients at transitions from deep to shallow flow.

These locations may or may not coincide with crevasse fields that exist during quiescent phase. The Khitrov crevasses and icefalls around the Grindle Corner are always present. During the surge the crevasse types in these areas become more complex resulting in multidirectional and chaotic crevasse patterns. A similar process has been observed at the lower end of topographic spurs in the Bagley Ice Field where en échelon crevasses form when the kinematic wave of the surge results in crevassing in areas of previously damaged material. There, the direction of the surge force can be distinguished from the direction that formed the topographically induced crevasse field (Herzfeld & Mayer, 1997). The reason is that part of the force (or kinematic energy) is needed to initiate the transition from an undamaged to damaged material state, while the remaining energy leads to formation of larger crevasses in the broken material. At the other end of the scale, we observe that the region of uncrevassed ice in the center of Bering Glacier corresponds to the region where the glacier is thickest and gradients of bedrock height are less steep compared to locations where the largest crevasses were observed.

A map comparison of BBGS's ice thickness (Figure 5c), and the natural logarithm of the mean *pond* value, derived from the 15 April 2011 Landsat-7 image, is shown in Figure 5d. We see very low values throughout the glacier indicating a good similarity between input glacier thickness and observed roughness. This indicates that input glacier bed topography is a major control in modeled and observed surface crevassing. However, the detail of the analysis that links bed topography, thickness, and crevassing is limited by the coverage of the region with bedrock observations. The most effective way to improve model-data comparison, and thus modeling of crevassing, would be through the collection of additional bedrock height measurements.

9. Discussion

9.1. Simulation of Observed Crevasses

Model-data comparison methods 1 and 2, comparing crevasse location and orientation, provide two scalar measures to evaluate our ability to numerically simulate observed, surge-induced crevasse fields. The first measure, α_1, indicates that crevasses locations are correctly simulated in 87.85% of the study domain. The large-scale acceleration during the surge has led to crevassing in many places throughout the study area which is captured by the model; however, the model's ability to also match locations of no crevassing is more notable, especially given the uniformity of our friction law. Disagreement of model- and data-based crevasse locations is generally explained by the lack of inclusion of inflowing glaciers in the model, which exist along the northern margin of Central Bering Glacier, for example, Betge Glacier (see Figure 1).

Crevasse orientations are closely aligned with the modeled axes of maximum principal stress in most places indicating that crevasse orientations of newly formed crevasses can be used to infer information about the surface stress regime. Visual inspection of Figure 6b shows that the model captures orientations quite well for the large crevasses in the Tashalich Arm area, in the eastern portion of the Khitrov Crevasses and along the southern margin of Central Bering Glacier. Orientations determined by model and data are assigned to the same directional bin ($\theta \leq 11.25^{\circ}$) along the southern margin of Central Bering Glacier, where no significant inflowing glaciers are present. This indicates that the lateral boundary condition well represents the surface stresses experienced along the southern margin during the early-2011 surge phase. The same-bin crevasse orientation agreement in Tashalich Arm and at the eastern edge of the Khitrov crevasse field, where large bedrock height gradients exist, indicates that these crevasses were formed purely from tensile extension.

On the other hand, there are many regions where orientations differ by more than three bins ($\theta > 33.75^{\circ}$). Many of these areas of orientation disagreement occur at boundaries of crevasse provinces, such as the isolated yellow points in the glacier lobe in Figure 6b, or in areas that have complex, multidirectional crevasses, such as those in the western Khitrov crevasse field or at the Grindle Corner. The orientation disagreement in the upper part of the study area may be explained by the fact that those crevasses may have formed in 2008–2009 during the acceleration event that preceded the 2011 phase (Burgess et al. (2013)).

These crevasses may have been rotated and transported during the early-2011 surge phase, and hence, we do not attempt to match this region with respect to orientation during our model optimization. Similarly, the discrepancy between the magnitudes of the von Mises stress and the mean *pond* value in southern Tashalich Arm is likely due to fast transport of large crevasses, which originally formed at the split of the main Central Bering Glacier bedrock trough into two branches, during the early-2011 phase of the surge.

9.2. Input Data Constraints

This study has used the best data available in early-2011. Landsat-7 data were selected since Landsat-8 was not launched until February 2013. Additionally, Worldview data were not chosen since 6 months worth of images were needed to cover Bering Glacier during the surge in 2011, and during this time surface characteristics changed significantly because of the surge.

Our analysis has also revealed several open problems both in the data constraints and in the modeling approach. To initialize the model's surface topography, we use a DEM derived from CryoSat-2 altimeter data. These measurements are the only altimeter data with sufficient spatial and temporal coverage collected during the surge. However, CryoSat-2 Level-2 data processing is complicated by the presence of crevasses throughout the glacier. This leads to unrealistically high modeled surface stresses at several locations. We reduce these effects by allowing the model to "relax" for 20 1-day time steps, but processing artifacts still exist. Additionally, the Landsat-7 satellite imagery, used for mapping surface structures, is limited by artificial stripes and suboptimal resolution. Finally, motivated by the conclusion that surface expressions during a surge are closely related to the bedrock topography, knowledge of bedrock structure needs to be significantly improved. Current bed topographic data sets lack coverage and more densely surveyed bed topography can be expected to lead to better model results.

9.3. Modeling Outlook

In the BBGS model, the linear friction law is uniformly applied throughout the entire model domain including all of Bering Glacier and the Eastern Bagley Ice Field. This is a simplification, in particular for the Bagley Ice Field whose bed is at a higher elevation and where there is less melt. The current model yields correct velocities near an imaginary line that connects the Grindle Corner and the Khitrov Hills but overestimates velocities and stresses up-glacier of this line and underestimates them down-glacier of this line. Additionally, the current model does not account for the presence of inflowing glaciers joining Central Bering Glacier in the model domain, yet these glaciers appear to have influences on the surge dynamics especially in terms of shear stresses along the lateral boundary. This motivates a future approach that optimizes the unknown model parameters, such as the basal friction and ice yield strength, on a node-by-node basis with some regularization by minimizing aggregated differences in the model-data comparisons. In addition, the lateral friction coefficient may be included in optimization to reduce edge effects of the homogeneous lateral boundary.

10. Summary and Conclusions

The study of the surge phenomenon is motivated by the fact that glacial acceleration is a major uncertainty in sea level rise prediction. Much of our communal understanding of glacier surging has been based on studies conducted on small glaciers. Thus, the surge of the BBGS, Earth's largest temperate surging system, in 2011–2013 has provided a unique opportunity to observe and analyze the surge phenomenon in a large and complex glacier system. During a surge, a glacier experiences rapid and large-scale acceleration associated with elevation changes and widespread crevassing. In this paper, we have introduced an approach that employs crevassing as a means to analyze ice dynamics and surface structures during a surge, using both numerical modeling and geostatistical data analysis.

The analysis focuses on three objectives: (1) to simulate the observed crevassing formed during the early-2011 phase of the BBGS surge, (2) to demonstrate that crevassing can be analyzed as a means to understand the physical processes of glacial acceleration through numerical modeling and novel crevasse-based model-data comparison techniques, and (3) to investigate the state of the BBGS during the acceleration phase in early-2011.

To meet objective 1, a 3-D full-Stokes finite element model of the BBGS is developed and applied to simulate ice flow and crevasse formation. The model is constrained using a surface DEM calculated from CryoSat-2 SIRAL data and a bed DEM from ice-penetrating radar data collected by NASA's Jet Propulsion Laboratory. Application of a von Mises stress criterion facilitates mapping of modeled crevasse locations.

Observation-based crevasse characterization is implemented by application of geostatistical methods and following the principles of structural glaciology. Parameterized spatial ice surface roughness is calculated from geostatistical functions applied to Landsat-7 image data and validated using field observations. The model-data comparison approach includes three quantitative and spatial measures of crevasse similarity with respect to location, orientation, and crevassity.

Comparison of modeled and data-based crevasse locations demonstrates that the model is able to reproduce observed crevassing in 85.75% of locations within our study area. Model-data orientations agree to within the resolution of the study (11.25°) along Bering Glacier's southern margin and at locations of large gradients in bedrock height. Because both metrics show high similarity between modeled and mapped crevassing, we conclude that the model has the ability to represent the BBGS system during the peak acceleration phase in early-2011, and thus, objective 1 has been met. However, the areas where orientations differ by more than 33.75° indicate that the model could be improved, for example, by including inflowing glaciers, modeling crevasse transport, or by collection of additional bedrock topographic data.

In addition, the crevasse-based approach is employed to optimize the ice stress threshold in the von Mises criterion and the basal friction coefficient simultaneously (for a linear friction law that is deemed adequate considering the complexity of the system and the data constraints and distributions). Model runs using the optimized parameters have led to the results summarized above.

More generally, the work in this paper has resulted in a framework that includes a numerical model of the BBGS during the acceleration phase of the surge, a crevasse characterization method that can be applied to satellite image data, and evaluation metrics to asses model-data comparison. Specifically, we have demonstrated that the crevasse-based approach can be applied in modeling the surge process and in evaluation of model quality (objectives 2 and 3). Application of the map comparison method to detailed analysis of locations of crevasse formation, as indicated by the geostatistical characterization (mean *pond* parameter), and ice thickness shows that bed topography plays an important role as a control of crevasse distribution and magnitude during the surge process. The framework developed here sets the stage for future advances in all three groups of data analysis, modeling, and model-data comparison. Envisioned next steps concern a model of the entire surge period 2011–2013 and application of an encompassing suite of crevasse classification parameters to higher resolution image data.

Acknowledgments

Thanks are due to our BBGS campaign pilot, Terry Kennedy, and to Katie and Tom Prijatel of Alaska Wilderness Air, Cordova, for flight support, to Bruce Molnia, U.S. Geological Survey, for alerting the second author of the start of the surge in June 2011, to Ralf Greve (Institute of Low Temperature Science, Hokkaido University, Sapporo, Japan) for discussions on modeling surging and ice dynamics, to Eric Rignot (Jet Propulsion Laboratory, Pasadena, USA) and Jeremie Mouginot (University California Irvine, USA) for sharing their bed topographic data, to Brian McDonald and Maciej Stachura (University of Colorado Boulder, USA) for help with field data collection in 2011–2013, to Griffin Hale (CU Boulder) and Almut Herzfeld Mayer for help during the summer field campaign 2012, and to Anders Damsgaard (Geophysical Fluid Dynamics Laboratory, Program in Atmospheric and Oceanic Sciences, Princeton University, USA) for comments on the manuscript. Support of the research presented here through the U.S. National Science Foundation's (NSF) Arctic Natural Sciences Program (Award ARC-1148800), Research Experience for Undergraduates (Award ARC-1247839), through NSF Geography and Spatial Sciences (Award GSS-1553133) and through NASA Cryospheric Sciences (Awards NNX17AG75G and NNX15AC73G) is gratefully acknowledged. The Landsat-7 data used in this analysis were downloaded using the USGS Global Visualization Viewer (GloVis) found at https://glovis.usgs.gov/. The airborne imagery from our Fall 2011 Bering Glacier campaign shown in Figure 2 is found at http://eces.colorado.edu/BeringBagley/#/. Additional data collected during the Bering Glacier RAPID project are available via NSF's Arctic Data Center under the title "RAPID: Bering Glacier Surge–Observation, Analysis and Parameterization".

References

Bouffard, J. (2015). CRYOSAT-2: Level 2 product evolutions and quality improvements in Baseline C (v3).

Burgess, E. W., Forster, R. R., Larsen, C. F., & Braun, M. (2013). Surge dynamics on Bering Glacier, Alaska, in 2008–2011. *The Cryosphere*, *6*, 1251–1262.

Clarke, G. (1987). Fast glacier flow: Ice streams, surging, and tidewater glaciers. *Journal of Geophysical Research*, *92*, 8835–8842.

Clarke, G. K., Collins, S. G., & Thompson, D. E. (1984). Flow, thermal structure, and subglacial conditions of a surge-type glacier. *Canadian Journal of Earth Sciences*, *21*(2), 232–240.

Clason, C., Mair, D. W., Burgess, D. O., & Nienow, P. W. (2012). Modelling the delivery of supraglacial meltwater to the ice/bed interface: Application to southwest Devon Ice Cap, Nunavut, Canada. *Journal of Glaciology*, *58*(208), 361–374.

Crossen, K. J., & Lowell, T. V. (2010). Holocene history revealed by post-surge retreat: Bering glacier forelands, Alaska. *Geological Society of America Special Papers*, *462*, 235–250.

Cuffey, K., & Paterson, W. S. B. (2010). *The physics of glaciers* (4th ed., 693 pp.). New York: Elsevier.

Dolgushin, L., & Osipova, G. (1975). Glacier surges and the problem of their forecast. *Symposium on snow and ice in mountain regions*, *104*, 292–304.

Eisen, O., Harrison, W., Echelmeyer, K., Bender, G., & Gorda, J. (2005). Variegated glacier, Alaska, USA: A century of surges. *Journal of Glaciology*, *51*, 399–406.

Eisen, O., Harrison, W., & Raymond, C. (2001). The surges of variegated glacier, Alaska, USA, and their connection to climate and mass balance. *Journal of Glaciology*, *47*, 351–358.

Fatland, D. R., & Lingle, C. S. (1998). Analysis of the 1993-95 Bering Glacier (Alaska) surge using differential SAR interferometry. *Journal of Glaciology*, *44*(148), 532–546.

Fatland, D. R., & Lingle, C. S. (2002). In SAR observations of the 1993-95 Bering Glacier (Alaska, USA) surge and a surge hypothesis. *Journal of Glaciology*, *48*(162), 439–451.

Fleischer, P. J., Bailey, P. K., Natel, E. M., Muller, E. H., Cadwell, D. H., & Russell, A. (2010). The 1993–1995 surge and foreland modification, Bering Glacier, Alaska. *Geological Society of America Special Paper*, *462*, 193–216.

Flowers, G. E., & Clarke, G. (2000). An integrated modelling approach to understanding subglacial hydraulic release events. *Annals of Glaciology*, *31*, 222–228.

Flowers, G. E., & Clarke, G. (2002a). A multicomponent coupled model of glacier hydrology, 1. Theory and synthetic examples. *Journal Geophysical Research*, *107*(B11), 2287. https://doi.org/10.1029/2001JB001122

Flowers, G. E., & Clarke, G. (2002b). A multicomponent coupled model of glacier hydrology, 2. Application to Trapridge Glacier, Yukon, Canada. *Journal Geophysical Research*, *107*(B11), 2288. https://doi.org/10.1029/2001JB001124

Flowers, G. E., Roux, N., Pimentel, S., & Schoof, C. G. (2011). Present dynamics and future prognosis of a slowly surging glacier. *The Cryosphere*, *5*, 299–313.

Forster, R. R., Rignot, E., Sacks, B. L., & Jezek, K. C. (1999). Interferometric radar observations of glaciares Europa and penguin, Hielo Patagonico Sur, Chile. *Journal of Glaciology*, *45*(150), 325–337.
Gagliardini, O., Zwinger, T., Gillet-Chaulet, F., Durand, G., Favier, L., et al. (2013). Capabilities and performance of Elmer/Ice, a new-generation ice sheet model. *Geoscientific Model Development*, *6*(4), 1299–1318.
Glen, J. W. (1955). The creep of polycrystalline ice. In *Proceedings of the royal society of London A: Mathematical, Physical and Engineering Sciences* (Vol. 228, pp. 519–538). The Royal Society.
Greve, R. (2003). *Kontinuumsmechanik*. Berlin Germany: Springer.
Harper, J. T., Humphrey, N., & Pfeffer, W. T. (1998). Crevasse patterns and the strain-rate tensor: A high-resolution comparison. *Journal of Glaciology*, *44*(146), 68–76.
Harrison, W., Motyka, R., Truffer, M., Eisen, O., Moran, M., Raymond, C., et al. (2008). Another surge of variegated glacier, Alaska, USA, 2003/04. *Journal of Glaciology*, *54*(184), 192–194.
Harrison, W., & Post, A. (2003). How much do we really know about glacier surging? *Annals of Glaciology*, *36*(1), 1–6.
Herzfeld, U. (1998). *The 1993–1995 surge of Bering Glacier (Alaska)—A photographic documentation of crevasse patterns and environmental changes, Trierer Geograph. Studien*. (Vol. 17, 211 pp.). Germany: Geograph. Gesellschaft Trier and Fachbereich VI – Geographie/Geowissenschaften, Universität Trier.
Herzfeld, U. C. (2004). *Atlas of Antarctica: Topographic maps from geostatistical analysis of satellite radar altimeter data* (Vol. 1, 364 pp.). Berlin, Heidelberg: Springer Verlag.
Herzfeld, U. C. (2008). Master of the obscure—Automated geostatistical classification in presence of complex geophysical processes. *Mathematical Geosciences*, *40*(5), 587–618. https://doi.org/10.1007/s11004-008-9174-4
Herzfeld, U. C., Clarke, G. K. C., Mayer, H., & Greve, R. (2004). Derivation of deformation characteristics in fast-moving glaciers. *Computers & Geosciences*, *30*(3), 291–302.
Herzfeld, U. C., & Mayer, H. (1997). Surge of Bering Glacier and Bagley ice field, Alaska: An update to August 1995 and an interpretation of brittle-deformation patterns. *Journal of Glaciology*, *43*(145), 427–434.
Herzfeld, U. C., McDonald, B., Stachura, M., Hale, R. G., Chen, P., & Trantow, T. (2013). Bering Glacier surge 2011: Analysis of laser altimeter data. *Annals of Glaciology*, *54*(63), 158–170. https://doi.org/10.3189/2013AoG63A348
Herzfeld, U. C., McDonald, B., Wallin, B. F., Krabill, W., Manizade, S., Sonntag, J., et al. (2014). Elevation changes and dynamic provinces of Jakobshavn Isbræ, Greenland, derived using generalized spatial surface roughness from ICES at GLAS and ATM data. *Journal of Glaciology*, *60*(223), 834–848.
Herzfeld, U., McDonald, B., & Weltman, A. (2013). Bering Glacier and bagley ice valley surge 2011: Crevasse classification as an approach to map deformation stages and surge progression. *Annals of Glaciology*, *54*(63), 279–286. https://doi.org/10/3189/2013AoG63A338
Herzfeld, U. C., & Merriam, D. F. (1990). A map comparison technique utilizing weighted input parameters. *Computers & Geology*, *7*, 43–52.
Herzfeld, U. C., & Zahner, O. (2001). A connectionist-geostatistical approach to automated image classification, applied to the analysis of crevasse patterns in surging ice. *Computers & Geosciences*, *27*(5), 499–512.
Holdsworth, G. (1965). *An examination and analysis of the formation of transverse crevasses*. Yukon Territory, Canada: Kaskawulsh Glacier.
Holdsworth, G. (1969). Primary transverse crevasses. *Journal of Glaciology*, *8*(52), 107–129.
Hubbard, A., & Hubbard, B. (2000). The potential contribution of high-resolution glacier flow modelling to structural glaciology. *Geological Society, London Special Publications*, *176*(1), 135–146.
Humphrey, N., Raymond, C., & Harrison, W. (1986). Discharges of turbid water during mini-surges of Variegated Glacier, Alaska, U. S. A.*Journal of Glaciology*, *32*(111), 195–207.
Jay-Allemand, M., Gillet-Chaulet, F., Gagliardini, O., & Nodet, M. (2011). Investigating changes in basal conditions of Variegated Glacier prior to and during its 1982–1983 surge. *The Cryosphere*, *5*(3), 659–672. https://doi.org/10.5194/tc-5-659-2011
Jiskoot, H. (1999). Characteristics of surge-type glaciers (PhD thesis).
Josberger, E. G., Shuchman, R. A., Meadows, G. A., Savage, S., & Payne, J. (2010). Hydrography and circulation of ice-marginal lakes at Bering Glacier, Alaska, USA. *Geological Society of America Special Paper*, *462*, 67–82.
Kamb, W., Raymond, C., Harrison, W., Engelhardt, H., Echelmeyer, K., Humphrey, N., et al. (1985). Glacier surge mechanism: 1982–1983 surge of Variegated Glacier, Alaska. *Science*, *227*(4686), 469–479.
Kehle, R. O. (1964). Deformation of the Ross ice shelf, Antarctica. *Geological Society of America Bulletin*, *75*(4), 259–286.
Larour, E., Utke, J., Csatho, B., Schenk, A., Seroussi, H., Morlighem, M., et al. (2014). Inferred basal friction and surface mass balance of North-East Greenland Ice Stream using data assimilation of ICES at-1 surface altimetry and ISSM. *The Cryosphere Discussions*, *8*(3), 2331–2373. https://doi.org/10.5194/tcd-8-2331-2014
Lingle, C., Post, A., Herzfeld, U. C., Molnia, B. F., Krimmel, R., & Roush, J. (1993). Bering Glacier surge and iceberg-calving mechanism at Vitus Lake, Alaska, USA. *Journal of Glaciology*, *39*, 722–727.
Liu, I. (2002). *Continuum mechanics* (297 pp.). Berlin: Springer.
MacAyeal, D. R. (1992). The basal stress distribution of Ice Stream E, Antarctica, inferred by control methods. *Journal of Geophysical Research*, *97*(B1), 595–603.
Markham, B. L., Storey, J. C., Williams, D. L., & Irons, J. R. (2004). Landsat sensor performance: History and current status. *IEEE Transactions on Geoscience and Remote Sensing*, *42*(12), 2691–2694.
Massonnet, D., & Feigl, K. L. (1998). Radar interferometry and its application to changes in the Earth's surface. *Reviews of Geophysics*, *36*(4), 441–500.
Mayer, H., & Herzfeld, U. (2000). Structural glaciology of the fast-moving Jakobshavn Isbræ, Greenland, compared to the surging Bering Glacier, Alaska, USA. *Annals of Glaciology*, *30*(1), 243–249.
Means, W. (1976). *Stress and strain: Basic concepts of continuum mechanics for geologists* (339 pp). New York: Springer.
Meier, M., & Post, A. (1969). What are glacier surges? *Canadian Journal of Earth Sciences*, *6*(4), 807–817.
Messerli, A., & Grinsted, A. (2015). Image georectification and feature tracking toolbox: ImGRAFT. *Geoscientific Instrumentation Methods and Data Systems*, *4*(1), 23.
Molnia, B. F. (2008). Alaska, satellite image atlas of glaciers of the world, 525 pp., U.S. Geological Survey Professional Paper 1386-K, Washington, DC.
Molnia, B., & Post, A. (1995). Holocene history of Bering Glacier, Alaska: A prelude to the 1993–1994 surge. *Physical Geography*, *16*(2), 87–117.
Molnia, B. F., & Post, A. (2010). Introduction to the Bering Glacier system, Alaska/Canada: Early Observations and scientific investigations, and key geographic features. *Geological Society of America Special Paper*, *462*, 13–42.
Molnia, B., & Williams, R. (2001). *Glaciers of Alaska* (Vol. 28-2, 112 pp.). Alaska Geographic Society.

Morlighem, M., Rignot, E., Seroussi, H., Larour, E., Ben Dhia, H., & Aubry, D. (2010). Spatial patterns of basal drag inferred using control methods from a full-Stokes and simpler models for Pine Island Glacier, West Antarctica. *Geophysical Research Letters*, *37*, L14502. https://doi.org/10.1029/2010GL043853

Poinar, K., Joughin, I., Das, S. B., Behn, M. D., Lenaerts, J., & Broeke, M. R. (2015). Limits to future expansion of surface-melt-enhanced ice flow into the interior of western Greenland. *Geophysical Research Letters*, *42*(6), 1800–1807. https://doi.org/10.1002/2015GL063192

Post, A. (1969). Distribution of surging glaciers in western North America. *Journal of Glaciology*, *8*(53), 229–240.

Post, A. (1972). Periodic surge origin of folded medial moraines on Bering Piedmont Glacier, Alaska. *Journal of Glaciology*, *11*(62), 219–226.

Ramsay, J., & Lisle, R. (2000). *The techniques of modern structural geology, Vol. 3: Applications of continuum mechanics in structural geology*. (7011061 pp.). San Diego, CA: Academic Press.

Raymond, C. (1987). How do glaciers surge? A review. *Journal of Geophysical Research*, *92*(B9), 9121–9134.

Rignot, E., Mouginot, J., Larsen, C., Gim, Y., & Kirchner, D. (2013). Low-frequency radar sounding of temperate ice masses in Southern Alaska. *Geophysical Research Letters*, *40*, 5399–5405. https://doi.org/10.1002/2013GL057452

Roush, J. J., Lingle, C. S., Guritz, R. M., Fatland, D. R., & Voronina, V. A. (2003). Surge-front propagation and velocities during the early-1993-95 surge of Berring Glacier, Alaska, U. S. A., from sequential SAR imagery. *Annals of Glaciology*, *36*, 37–44.

Seroussi, H., Morlighem, M., Rignot, E., Larour, E., Aubry, D., Ben Dhia, H., & Kristensen, S. S. (2011). Ice flux divergence anomalies on 79north Glacier, Greenland. *Geophysical Research Letters*, *38*, L09501. https://doi.org/10.1029/2011GL047338

Sevestre, H., & Benn, D. I. (2015). Climatic and geometric controls on the global distribution of surge-type glaciers: Implications for a unifying model of surging. *Journal of Glaciology*, *61*(228), 646–662.

Shuchman, R., & Josberger, E. G. (2010). Bering Glacier: Interdisciplinary studies of Earth's largest temperate glacier. *Geological Society of America Special Paper*, *462*, 384.

Shuchman, R. A., Josberger, E. G., Jenkins, L. K., Payne, J. F., Hatt, C. R., & Spaete, L. (2010). Remote sensing of the Bering Glacier region. *Geological Society of America Special Paper*, *462*, 43–66.

Stocker, T. F., Qin, H., Plattner, G.-K., Tignor, M., Allen, S. K., Boschung, J., et al. (2013). *Climate change 2013: The physical science basis. Contribution of Working Group I to the Fifth Assessment Report of the Intergovernmental Panel on Climate Change*. Cambridge: Cambridge University Press.

Suppe, J. (1985). *Principles of structural geology* (573 pp.). Englewood Cliffs, NJ: Academic Press.

Trantow, T. (2014). Numerical experiments of dynamical processes during the 2011–2013 surge of the Bering-Bagley Glacier System using a full-Stokes finite element model (Master's thesis). University of Colorado.

Trantow, T., & Herzfeld, U. (2016). Spatiotemporal mapping of a large mountain glacier from CryoSat-2 altimeter data: Surface elevation and elevation change of Bering Glacier during surge (2011–2014). *International Journal of Remote Sensing*, *37*(13), 2962–2989.

Truffer, M., & Echelmeyer, K. A. (2003). Of isbrae and ice streams. *Annals of Glaciology*, *36*(1), 66–72.

Turrin, J., Forster, R. R., Larsen, C., & Sauber, J. (2013). The propagation of a surge front on Bering Glacier, Alaska, 2001–2011. *Annals of Glaciology*, *54*(63).

Twiss, R., & Moore, E. (1992). *Structural geology* (532 pp.). New York: W.H. Freeman.

Van der Veen, C. (1998). Fracture mechanics approach to penetration of surface crevasses on glaciers. *Cold Regions Science and Technology*, *27*(1), 31–47.

Van der Veen, C. (1999). Crevasses on glaciers 1. *Polar Geography*, *23*(3), 213–245.

Vaughan, G. (1993). Relating the occurrence of crevasses to surface strain rates. *Journal of Glaciology*, *39*(132), 255–266.

Zwinger, T., & Moore, J. (2009). Diagnostic and prognostic simulations with a full Stokes model accounting for superimposed ice of Midtre Lovénbreen, Svalbard. *The Cryosphere*, *3*(2), 217–229.